AN ABSTRACT OF THE THESIS OF

Changho Choi for the degree of Master of Science in Chemical Engineering presented on October 13, 2009.

Title: Fabrication and Characterization of Nanostructured Surfaces for Enhanced Heat Transfer

Abstract approved:

<hr>

Chih-Hung Chang

This objective of this study is to investigate the capability of nanostructured surfaces on dissipating heat flux by performing pool boiling and convective flow boiling. The generation of ultra-high heat flux from high performance electric devices has motivated a number of investigations related to advanced heat transfer especially in two-phase boiling performance. It has been reported by a number of researchers that nanostructured surfaces can result in much enhanced boiling performance, compared to the conventional methods by creating desire conditions for heat transfer. In this thesis, various nanostructured surfaces having different morphology were prepared on several engineering relevant substrates and were characterized for their pool boiling performance. Microreactor-assisted-nanomaterial-deposition, MAND^{TM} was used to fabricate a variety of different ZnO nanostructured surfaces by careful adjustment of the processing parameters. ZSM-5 zeolite was synthesized using hydrothermal reaction. ZnO nanostructures in minichannel were also successfully deposited via a

flow cell for the application of flow boiling experiment. Scanning electron microscopy (SEM) and Atomic Force Microscopy (AFM) were carried out to characterize the micro- and nanostructures. Contact angle measurement was conducted to evaluate wettability and X-ray Diffraction (XRD) was used to determine the crystalline structures. The most significant enhancement of critical heat flux (CHF) and heat transfer coefficient (HTC) was observed in the flower like ZnO nanostructured surface. We observed pool boiling CHF of 80-82.5 W/cm^2 for nanostructured ZnO on Al surfaces versus a CHF of 23.2 W/cm^2 on a bare Al surface with a wall superheat reduction of 25-38°C. This new CHF values on nanostructured surfaces corresponds to a boiling heat transfer coefficient as high as ~ 23000 W/m^2K. This represents an increase of almost 4X in CHF on nano-textured surfaces, which is the highest enhancement factor reported today.

Fabrication and Characterization of Nanostructured Surfaces for Enhanced Heat Transfer

by
Changho Choi

A THESIS

submitted to

Oregon State University

in partial fulfillment of
the requirements for the
degree of

Master of Science

Presented October 13, 2009
Commencement June 2010

Master of Science thesis of <u>Changho Choi</u> presented on <u>October 13, 2009</u>.

APPROVED:

_____

Major Professor, representing Chemical Engineering

_____

Head of the School of Chemical, Biological & Environmental Engineering

_____

Dean of the Graduate School

I understand that my thesis will become part of the permanent collection of Oregon State University libraries. My signature below authorizes release of my thesis to any reader upon request.

_____

Changho Choi, Author

ACKNOWLEDGEMENTS

TABLE OF CONTENTS

LIST OF FIGURES

LIST OF FIGURES (Continued)

LIST OF TABLES

NOMENCLATURE

<u>Symbol</u>

Nu	Nusselt number
b	bubble
l	liquid
h	heat transfer coefficient
L	hydrodynamic length
k	thermal conductivity
Re	Reynolds number
v	vapor
μ	viscosity
Θ	contact angle
g	gravity
σ	surface tension
q"	heat flux per area
T	temperature
w	surface wall
P	pressure
C_{pl}	liquid specific heat
a	thermal diffusivity
ρ	density
Pr	Prandtl number
U	velocity
k	thermal conductivity
t	time

1 Introduction

1.1 Motivation and background

High performance electronic devices such as advanced very large-scale integration (VLSI) technology have advanced significantly in the past decades. With the trend of compact and light-weight devices, the demand of heat flux dissipation has increased tremendously in particularly for high performance equipment which generates heat flux up to several hundred or even thousand W/cm^2 levels.

There are two major types of heat transfer techniques, passive and active. The active methods involve external power equipment to accelerate the heat removal such as fans and evaporative air conditioner. This method is less attractive than the passive technique because of its more complicated design and the space limit for the cooling facility. On the other hand, passive methods, not requiring any external power input, have been intensively researched in the past decades. The advantage of a passive method is the capability of being compact, cost efficient, and enhanced heat transfer. A review of passive methods has been published [1]. Among the various passive methods, two-phase cooling systems using the latent heat during the phase change have been considered as one of the most promising approaches to dissipate large amount of heat flux due to their nature, in that enormous amounts of heat can be transferred as the phase change from liquid to vapor occurs.

Pool boiling along with convective flow boiling has drawn significant interest to its convenience and inexpensive experimental facility to implement. The

characterization of boiling performance that has been reported by a number of researchers has deduced one conclusion that heat transfer enhancement could be established by the modification of the boiling surface. A variety of surface treatment methods have been employed to modify the morphology of the boiling surface in a hope of yielding high heat dissipation [2-5]. Recently nanotechnology has appeared as a prominent technique for advanced heat transfer capability, providing a more effective boiling surface for advanced boiling heat transfer. Bang et al. investigated boiling heat transfer characteristics using Al_2O_3 nano-particles suspended in water as a coolant. They showed that critical heat flux (CHF) has been improved regardless of the orientation of the heater whereas heat transfer coefficient (HTC) is declined compared to that obtained using pure water [6]. Kim et al. also performed the boiling experiment using TiO_2 or Al_2O_3 nano-fluids to investigate the CHF characteristics of nano-fluids [7]. They proposed that the significant CHF enhancement is attributed to the surface modification created by nano-particle deposition on the substrate, which is consistent with the explanation demonstrated by former researchers who used conventional techniques to acquire the surface modification [2-5]. As another example of making surface modification associated with nanotechnology, Sebastine et al. fabricated carbon nanotube (CNT) on the heated surface to assess the impact of the CNT coating for pool boiling performance. The results indicated a fully coated surface with CNT is highly effective at enhancing the boiling performance in terms of reducing the incipience superheat as well as improving both CHF and HTC [8].

Two-phase convective flow boiling performance, which generally use microchannel as a heat sink, has also been significantly investigated to meet the demand of accommodating heat flux levels in the range of 1000-10,000 W/cm^2 [9, 10]. Appropriate models regarding flow boiling phenomena using microchannel have been studied to predict CHF and deal with some challenges such as hydrodynamic instability and pressure drop which are observed during two-phase flow boiling experiment [11~13]. In order to achieve more efficient heat transfer capability, various nanostructured surfaces which are favorable in heat transfer performance have been employed. Khanikar and Mudawar introduced a microchannel coated with carbon nanotubes (CNTs). They reported that CNTs had successfully coated to the bottom wall of a shallow rectangular microchannel by microwave plasma chemical vapor deposition chamber and showed CHF was enhanced at low mass velocities [14]. An enhanced heat transfer performance under forced convection was also achieved by adopting highly-wettable surface obtained by coating TiO_2 in annulus channel of a heater rod [15].

In this study, ZnO nanostructured surfaces having different morphologies were fabricated on polished metal substrates as well as on the bottom of minichannel for the application of pool boiling and convective flow boiling performance, respectively. In addition, the result of pool boiling performance, which was carried out prior to flow boiling experiment to demonstrate the effect of surface treatment, successfully showed the significant enhancement of heat transfer. This results in providing the inspiration

for conducting convective flow boiling experiment with the nanostructured surface in minichannel.

1.2 Pool boiling curve

Pool boiling typically entails a surface submerged in an extensive pool under the stagnant condition with heat transfer driven by buoyancy force. The first systematic characteristic of boiling behavior was carried out as Nukiyama explored the boiling phenomena on a horizontal nichrome wire, demonstrating the different regimes of pool boiling performance using boiling curve [16]. A plot of heat flux versus wall superheat under a certain circumstance is shown in Figure 1.1. In the ambient condition, the liquid in the pool is saturated. If the surface temperature of the immersed body is controlled and slowly increased, a typical boiling curve can be obtained like that of Figure 1.1. At very low superheat levels, no bubble nucleation is created and heat is transferred from the surface to the liquid by natural convection. If the superheat is great enough to initiate bubble nucleation, a few bubbles could be formed at some cavities on the surface, which is called onset of nucleate boiling. In the isolated bubble regime, a few individual bubbles are created and depart from cavities on the surface.
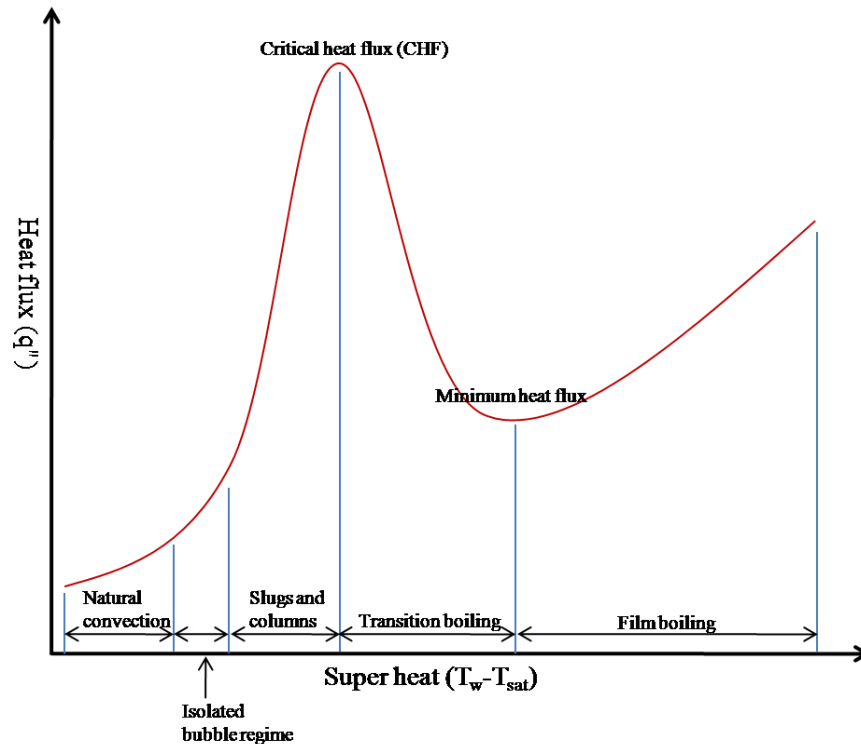
Figure 1.1 Pool boiling curve obtained by controlling surface temperature.

As more heat is supplied to the liquid, more cavities become active, and the bubble frequency at each cavity generally increase. Once the spacing between isolated bubbles is so close and there is a rapid increase of bubble frequency, bubbles from adjacent cavities merge together and eventually form vapor slugs or vapor columns. With increasing surface superheat in the region of vapor slugs and columns, vapor accumulates near the surface at some sites interfering with the inflow of the liquid into the surface, which eventually leads to dry out on some parts of the surface. Due to the fact that heat transfer coefficient in the vapor is significantly lower than one in the liquid, the overall heat flux from the surface to liquid is decreased. This reduction of heat flux results in a peak of heat flux during pool boiling performance, which is

referred to as critical heat flux (CHF). If the superheat is increased beyond the critical heat flux condition, overall heat flux continues to be reduced. This regime is referred to as the transition boiling regime. In this regime, dry portions on the surface are unstable, showing significant fluctuation which results from the irregularity of surface rewetting. If the transition boiling is continued with increasing superheat, the regime could reach to the point referred to as the film boiling regime. Stable vapor film is formed in this regime and acts like an insulation blanket. Within the film boiling regime, the heat flux monotonically increases with the increase of superheat. This is due to the increasing conduction and convection heat transfer as the temperature gradient between the surface and the vapor film increases. As for a reference, the schematic diagram of pool boiling regime is presented in Figure 1.2.
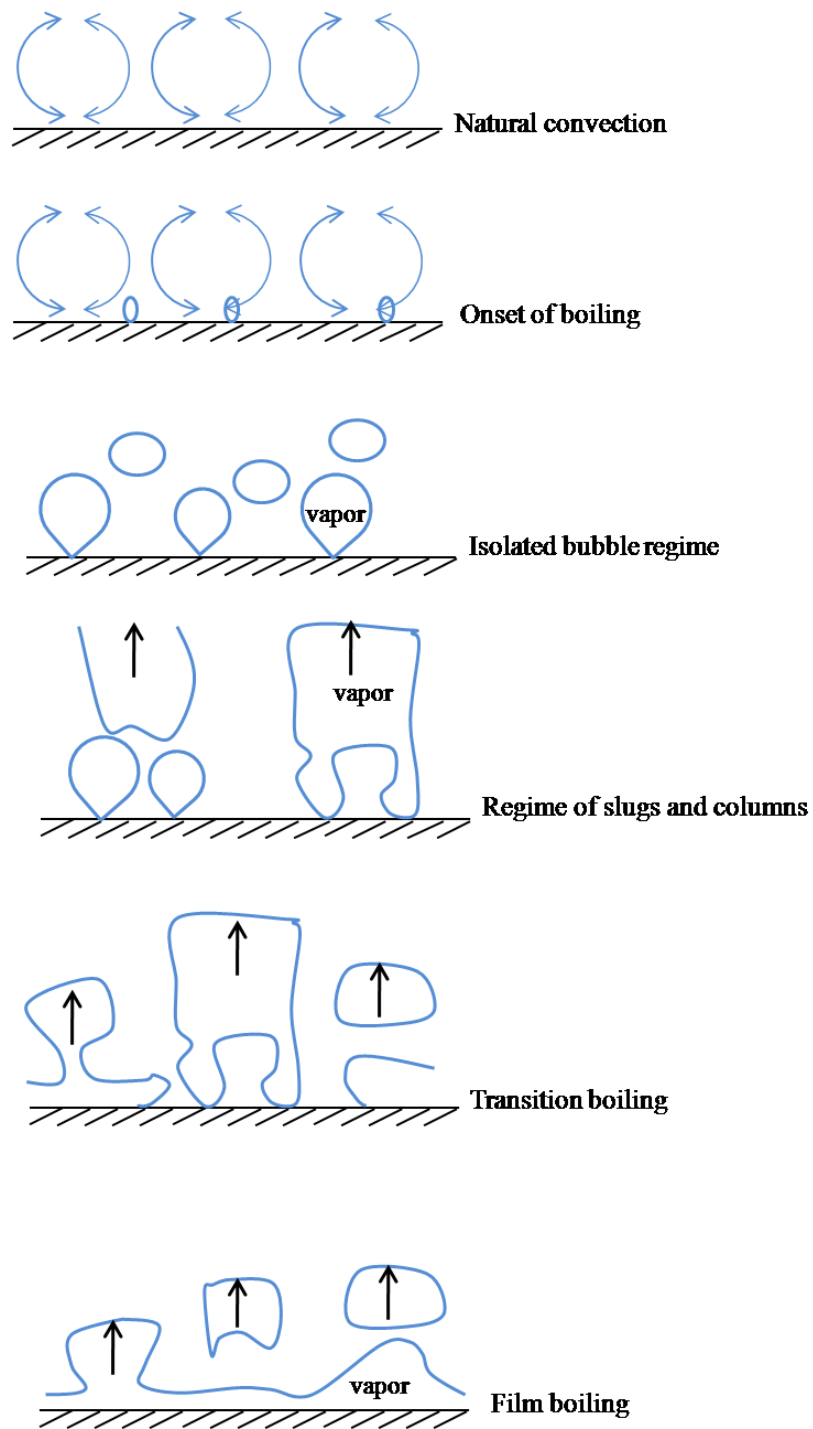
Figure 1.2 Schematic diagram of the regimes in pool boiling.

1.3 Mechanisms of bubble nucleation

Over the past 80 years, a number of investigations about the mechanism of the bubble nucleation have been intensively conducted because of its application in the various fields. A substantial number of mechanisms have been suggested so far, however, in this section a few of models which give good illustration on boiling nucleation are introduced.

1.3.1 Rohsenow's model

Rohsenow's model was proposed by Rohesnow in 1952 who assumed that single phase heat transfer correlation can be used to predict phase change heat transfer [17]. This reasoning is on the basis that the process of bubble nucleation is mainly attributed to the liquid agitation induced by bubble growth and bubble departure. The single phase heat transfer correlation begins the Reynolds number and Nusselt number [1.1a, b].

$$Nu_b = \frac{hL_b}{kl} = A \operatorname{Re}_b{}^n \operatorname{Pr}_l{}^m \qquad [1.1a]$$

$$\operatorname{Re}_b = \frac{\rho_v U_b L_b}{\mu_l} \qquad [1.1b]$$

Bubble departure diameter is correlated in order to identify L_b, appropriate bubble length scale [1.2a].

$$L_b = C_b \theta \left[\frac{2\sigma}{g(\rho_l - \rho_v)} \right]^{\frac{1}{2}} \qquad [1.2a]$$

$$U_b = \frac{q''}{\rho_v h_{lv}} \tag{1.2b}$$

where C_b is a constant that is specific to the system. U_b is determined from an energy balance [1.2b]. Re_b is defined as a ratio of vapor inertia to liquid viscous force. Heat transfer coefficient (h) is defined based on $T_{sat}(P_l)$ since experiments indicated that the effect of subcooling generally decreased rapidly with an increasing heat flux [1.3].

$$h = \frac{q''}{T_w - T_{sat}(P_l)} \tag{1.3}$$

With the substitution of above equations, Rohsenow's correlation is completed [1.4a].

$$\frac{q''}{\mu_l h_{lv}} \left[\frac{\sigma}{g(\rho_l - \rho_v)} \right]^{1/2} = \left(\frac{1}{C_{sf}} \right) Pr_l^{-s/r} \left[\frac{c_{pl}(T_w - T_{sat})}{h_{lv}} \right]^{1/r} \tag{1.4a}$$

$$C_{sf} = \frac{\sqrt{2} C_b \theta}{A} \tag{1.4b}$$

The constants r and s equal to 0.33 and 1.0 for water respectively. C_{sf} value is also varied with the combination of liquid and solid [1.4b]. For water on the polished surface, the value equals to 0.008.

1.3.2 Forster and Greif vapor-liquid exchange model

The vapor-liquid exchange model was proposed by Forster and Grief in 1959 [18]. This model is based on the premise that each bubble acts like micropumps driving cold fluid from the ambient toward the heated surface during bubble departure.

While bubbles grow, bubbles push the liquid near heated surface out into cooler ambient by single phase forced convection. They suggested sensible heat transfer, q_s, which is based on the assumption that each bubble pumps a quantity of liquid equal to its volume at bubble release [1.5].

$$q_s = \rho_{lc} p_l \left(\frac{2\pi}{3} \right) R_{max}^{\ 3} \left(\frac{T_w + T_l}{2} - T_l \right) f \qquad [1.5]$$

where R_{max} is a maximum bubble radius considered hemispherical shape, f is bubble frequency. If active nucleation site density is defined as $n_a{'}$, the above equation can be presented as following equation [1.6].

$$q_s = \rho_{lc} p_l \left(\frac{2\pi}{3} \right) R_{max}^{\ 3} \left(\frac{1}{2} \right) (T_w - T_l) f n_a{'} \qquad [1.6]$$

The sensible heat transfer correlation shown above suggests that T_w-T_l plays a significant role in terms of subcooling. However, in fact, experimental results indicated the right hand side of this correlation is independent of subcooling since R_{max} decreases with increasing subcooling while bubble frequency increases; Therefore, the net result is the sensible heat transfer is not dependent on subcooling, which indicates very little change in the right side of the correlation.

1.3.3 Mikic and Rohsenow model

Mikic and Rohsenow model was proposed in 1969 with premise that heat transfer rate is a result of combination of microconvection, which is resulting from the liquid-vapor exchange model and natural convection, which is existing between

bubbles in isolated bubble regime [19]. This model was described as the simple one-dimensional transient conduction process into a semi-infinite medium, consisting of two parts, the waiting period and the bubble growth period. The schematic diagram of waiting period is presented in Figure 1.3. The model to describe waiting period was analyzed along with appropriate governing heat equation, boundary, and initial condition [1.7a, b].
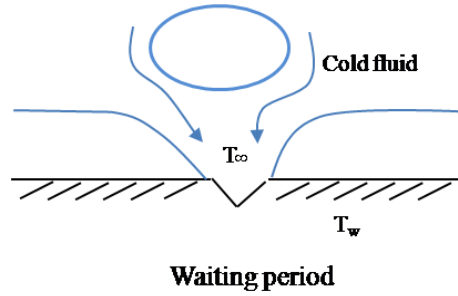
Figure 1.3 Schematic diagram of waiting period.

$$\frac{\partial T}{\partial t} = a_l \left(\frac{\partial^2 T}{\partial y^2} \right) \qquad\qquad [1.7a]$$

$$
\begin{aligned}
T\left(y, -t_w\right) &= T_\infty \\
T(\infty, t) &= T_\infty \\
T(0, t) &= T_w, -t_w \le t < 0
\end{aligned}
\qquad\qquad [1.7b]
$$

where $-t_W$ is defined as time prior to the bubble nucleation. The second model to explain the bubble growth period was also presented with schematic diagram as shown in Figure 1.4 [1.8a, b].
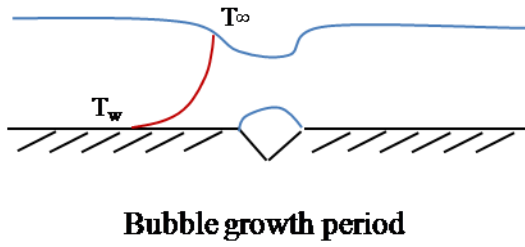
Figure 1.4 Schematic diagram of bubble growth period.

$$\frac{\partial T}{\partial t} = a_l \left(\frac{\partial^2 T}{\partial y^2} \right) \qquad [1.8a]$$

$$T(y,0) = T_f$$
$$T(\infty,t) = T_\infty \qquad [1.8b]$$
$$T(0,t) = T_{sat}(P_\infty), t > 0$$

where T_f is the temperature from waiting period at t=0, and T_{sat} means interface temperature. The analytical solution for above both equations is well interpreted with conjugated error function [1.9a].

$$T(y,t) = T_\infty + (T_w - T_\infty)erfc\left[\frac{y}{2\sqrt{a_l(t+t_w)}} \right] - (T_w - T_\infty)erfc\left[\frac{y}{2\sqrt{a_l t}} \right] \qquad [1.9a]$$

The heat transfer rate can be determined from above relation and shown below [1.10].

$$q''_{mc} = -k_l \left(\frac{\partial T}{\partial y} \right)_{y=0} = \frac{k_l \left[T_w - T_{sat}(P_l) \right]}{(\pi a_l t)^{1/2}} \qquad [1.10]$$

where q''_{mc} is heat flux in microconvection. If bubble frequency and average heat flux over a cycle of bubble growth and departure are applied to the above equation, the equation becomes as following equation [1.11].

$$\overline{q_{mc}''} = f\int_0^{1/f} q''_{mc}\,dt = \left(\frac{4k_l\rho_l c_{pl}}{\pi}\right)^{1/2}[T_w - T_{sat}(P_l)]f^{1/2} \qquad [1.11]$$

Total heat flux can be obtained by the area-weighted average of the microconvection and natural convection contribution [1.12].

$$q'' = \left(\frac{A_{mc}}{A_{tot}}\right)\overline{q''_{mc}} + \left(\frac{A_{nc}}{A_{tot}}\right)q''_{nc} \qquad [1.12]$$

If the natural convection term is considered so small compared to microconvection, the equation for total heat flux can be simplified ignoring natural convection term [1.13].

$$q'' = \left(\frac{A_{mc}}{A_{tot}}\right)\overline{q''_{mc}} = \left(\frac{\pi d_d^2}{4}\right)n_a'\overline{q''_{mc}} \qquad [1.13]$$

where $\pi d_d^2/4$ is the area of microconvection and n_a' is the number of bubble activation sites per unit area of surface. As a subsequent substitution of previous relations, total heat flux can be obtained as following equation [1.14].

$$q'' = 2(\pi k_l\rho_l c_{pl})^{1/2}f^{1/2}d_d^2 n_a'[T_w - T_{sat}(P_l)] \qquad [1.14]$$

This equation indicates that total heat flux is a function of bubble frequency, departure diameter, and active site density.

1.4 Critical heat flux models

The prediction of critical heat flux is extremely difficult due to its challenge of evaluating accurate important parameters such as bubble departure diameter and bubble frequency. Some appropriate models have been proposed and considered to somewhat enable interpretation of the bubble behavior and conditions near the critical heat flux. In this chapter, three different types of CHF mechanisms are briefly introduced.

1.4.1 Kutateladze model

Kutateladze proposed CHF model, considering the analogy between the CHF condition and flooding phenomena [20]. It was claimed by Kutateladze that bubbles coalesce near CHF and form a vapor column and if the velocity of the vapor column is so great to block the liquid droplets which are falling to the surface, a vapor blanket near the surface is created. This leads to the significant reduction of heat flux from the surface, rapidly increasing the superheat. The CHF model described by Kutateladze is following equation [1.15].

$$q''_{max} = C_k \rho_v^{1/2} h_{lv} [g(\rho_l - \rho_v)\sigma \;]^{1/4} \qquad\qquad [1.15]$$

where C_k is 0.131 for a flat heated surface of infinite extent.

1.4.2 Rohsenow and Griffith model

The mechanism, which is called the bubble packing mechanism, was introduced by Rohsenow and Griffith [21]. Their reasoning for this model is that when the number of nucleation sites increase near CHF with increase of superheat, a critical bubble packing is formed at the surface and inhibits the liquid inflow toward the surface. A vapor blanket is created, then preventing rewetting the surface.

1.4.3 Zuber and Lienhard model

Lienhard model was proposed on the basis of Zuber's CHF model, applying Helmholts instability [22]. The premise of this model is that when large vapor column becomes unstable due to the Helmholts instability which is caused by perturbed interface, CHF occurs. The instability results in distorting the vapor column and blocking liquid from effectively rewetting the surface as shown in Figure 1.5.
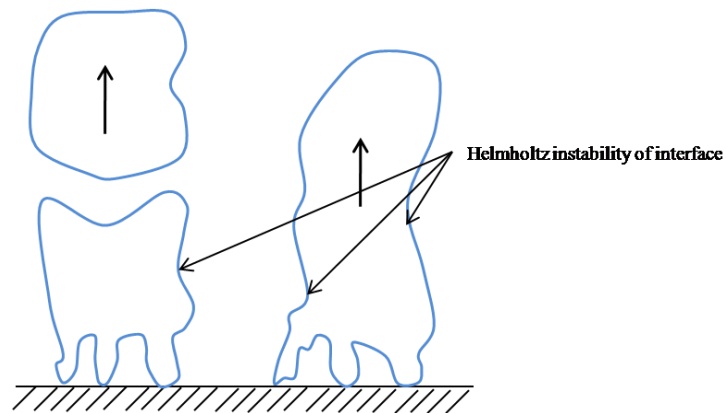
Figure 1.5 Helmholtz instability at CHF.

The CHF model proposed by Lienhard is following equation [1.16].

$$q''_{max} = 0.419 \rho_v h_{lv} \left[\frac{\sigma(\rho_l - \rho_v)g}{\rho_v^2} \right]^{1/4} \qquad\qquad [1.16]$$

1.5   Introducion to ZnO nanomaterias

ZnO nanostructures have been extensively investigated because of their unique properties that are useful for a wide range of applications such as nanodevices and photovoltaic cells [23, 24]. ZnO films can be synthesized using a variety of techniques and most interestingly a plethora of morphologies with unique micro and nanoscale features can be fabricated simply by modifying the growth parameters without the aid of additional patterning processes. Three major processes have been implemented for the synthesis of ZnO nanomaterials. The vapor-liquid-solid (VLS) mechanism uses vapor phase reactants and requires a catalyst to control the ZnO growth. Vapor-solid (VS) mechanism also uses vapor phase reactants however no catalysts are present for the synthesis of ZnO. Along with the other two vapor phase growth mechanisms, aqueous solution growth (ASG) mechanism offers a low cost and versatile route for the synthesis ZnO nanostructures. In the ASG mechanism, many experimental parameters can affect the morphology of the ZnO nanomaterial surface, so morphology control is more complicated than the other two mechanisms. By carefully tuning the process parameters in the ASG process, a variety of ZnO nanostructures have been obtained. These include ZnO nanotubes, nanorods, nanostacks, nanoplatelets, and nanoforests [23~26]. Some researchers have synthesized the flower

like ZnO structures and discussed that some of the process parameters such as pH level and reaction temperature and time can determine the ZnO morphology [24, 27]. Continuous flow method for synthesizing ZnO structures was introduced by Chih-Hung Chang et al. using MAND[TM] [28]. They demonstrated that various process parameters can result in various ZnO morphologies including flower like ZnO structure.

2   Fabrication and characterization of novel nanostructured surfaces

2.1   Experimental method for ZnO nanostructured surface

Micro-Assisted-Nanomaterial-Deposition (MAND^{TM}) was used to fabricate the ZnO nanostructured surfaces which are evaluated in this study. The unique property of using the MAND process is to obtain homogeneous ZnO film by adjusting some process parameters whereas the heterogeneous film is acquired through the conventional aqueous solution batch process. As presented in Figure 2.1, MAND system consists of a microprocessor controlled dispensing pump (Ismatec micropumps), a 1.22 mm ID Tygon ST tubing (Upchurch Scientific), a T-mixer (Upchurch scientific), a 3 in. diameter stainless steel metallic plate, and a 2 in diameter by 0.75 in. thick hotplate with a temperature controller (Watlow). In this experiment, the reactant streams, A and B, were initially pumped into the Tygon tube and allowed to mix in the T-mixer. Stream A consisted of 0.005M aqueous zinc acetate solution and 0.25M aqueous ammonium acetate solution. Stream B consisited of aqueous solution of sodium hydroxide (0.05M~0.1M). The solution mixture of A and B was passed through a 5ft long Tygon tube immersed in a water bath maintained at 70°C. The solution was then impinged on the substrate, which was placed on a 3 in. diameter stainless steel metallic disc rotating about 1500~2500 rpm and heated on a hot plate for desire temperature. The range of impinging time was from 2 to 10 min. Once the deposition process was complete, the substrate was removed from the plate and dried with a stream of nitrogen gas.

It was challenging to ensure the highly uniform coverage of ZnO nanoparticles on the large scale substrate. In this experiment, the substrate with 9.1cm^2 was coated with ZnO nanoparticles with high uniformity, demanding rigorous effort to determine the optimum process parameters including pH, resident time, and hot plate temperature. Indeed, the morphology of ZnO nanostructured surface as well as the extent of uniformity was strongly dependent on the process parameters, exhibiting different nanoparticle structures and varied uniformity.
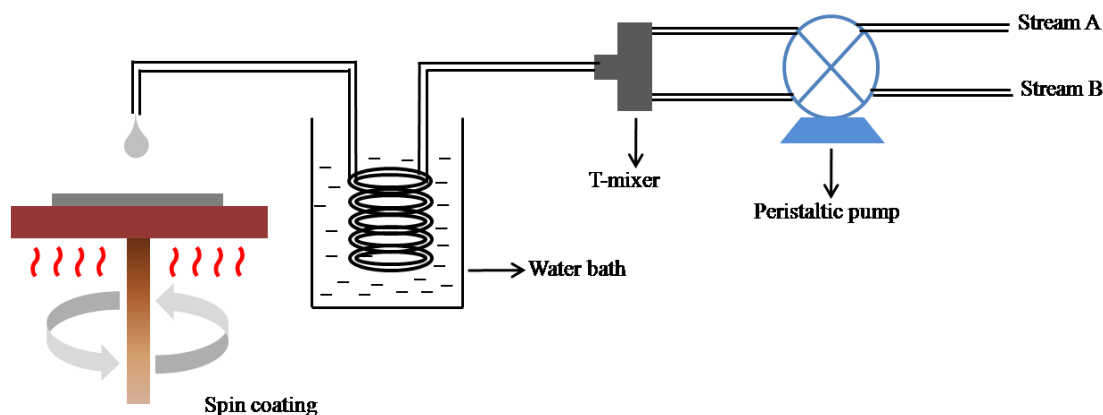
Figure 2.1 Schematic diagram of MAND^{TM}.

2.2   Synthesis of ZSM-5 type zeolite

ZSM-5 zeolite, which is composed with MFI type of framework, was synthesized for the application of pool boiling heat transfer. Zeolite generally consists of oxygen-sharing TO_4 where T is Si or Al. Zeolite has drawn significant attention over the past decades due to its unique property in that it consisted of a number of narrow pores with the range from 1 to 20Å. ZSM-5 is generally known as 6 Å pore size zeolite, and its framework (MFI) is shown in Figure 2.2.

It has been used in the various fields related to membrane and catalyst with excellent selectivity which results from its pore size and structure. Considering pore density of zeolite which possibly becomes bubble nucleation sites, this material is an excellent candidate application for pool boiling heat transfer. With this reasoning, ZSM-5 zeolite was synthesized on single crystal silicon substrate using hydrothermal reaction. The solution was made by gradually adding tetraethylorthosilicate (TEOS) into diluted aqueous tetrapropylammonium hydroxide (TPAOH) while stirring. The framework of the zeolite used in this study only consists of Si, which is called silicate zeolite. The molar ratio was 1 TEOS: 0.6 TPAOH: 165 DI water. 4g of mixed solution was loaded in hydrothermal reactor which is composed of Teflon material for interior and stainless for exterior part. ZSM-5 type of zeolite synthesis was carried out in the autoclave for 2 hours at 165 ℃. After the synthesis was completed, the surface was washed by DI water and dried out under nitrogen gas.
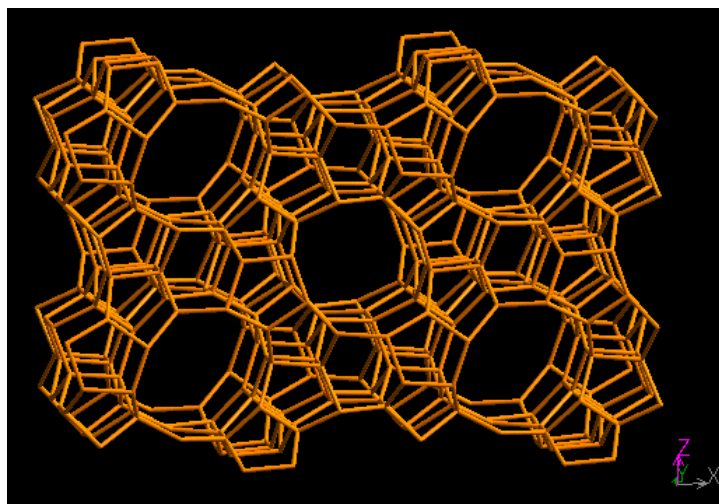
Figure 2.2 MFI framework image.

2.3   Characterization of nanostructured surfaces

2.3.1 Super-hydrophilic ZnO nanostructured surface on aluminum

A porous ZnO nanostructured surface was fabricated on aluminum substrates using MAND method as indicated in the previous section. Scanning Electron Microscopy (SEM) images of different magnification are presented along with SEM image of bare aluminum in Figure 2.3. The concentration of sodium hydroxide was 0.15M, which was the highest one among those that had been applied in this study. Volumetric flow rate was 8.28 ml/min that is corresponding to a 5 second residence time based on the tube diameter and length used in this study. The process parameters are summarized in .

A number of 1μm pores that are seemingly connected together from adjunct sites were observed from the SEM image. There are some key parameters which determine the efficacy of the pool boiling heat transfer performance. Surface roughness and surface wettability play significant roles in the boiling experiment. The contact angle measurement was used to evaluate the surface wettability. Lower contact angle implies that fluid can easily and constantly flow into the cavity after bubble release, which is very important in enhanced pool boiling heat transfer. A 2μL DI water droplet was placed on the ZnO nanostructured surface for the measurement of contact angle.

Table 2.1 MAND process parameters for super hydrophilic ZnO nanostructured surface

Type of ZnO surface	Concentration of NaOH (M)	Water bath temperature (°C)	Substrate holder temperature (°C)	Deposition time (min)	Rotating speed (rpm)	Flow rate (ml/min)
Super-hydrophilic	0.15	70	200	5	1500	8.28
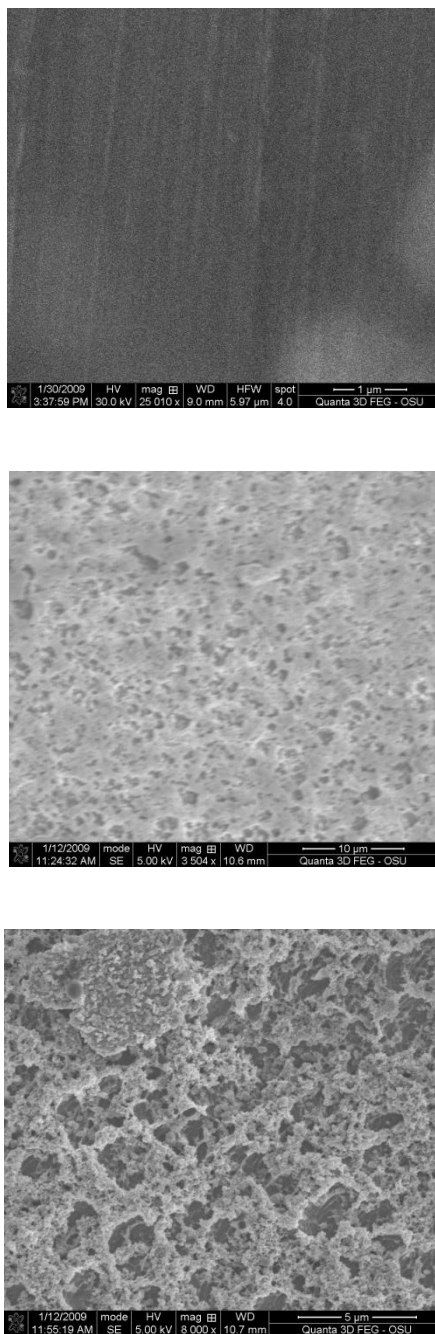
Figure 2.3 SEM images of bare aluminum (upper) and super-hydrophilic ZnO

nanostructured surface with different magnification (lower).

The shape of the droplet on the substrate was captured by high speed camera, and the contact angle was estimated by the captured image.

There are two models that are commonly used to explain the measured contact angle: Wenzel's model and Cassie's model [29]. Wenzel's model describes the case when the drop wets the groove on the surface whereas the drop sitting on the peak of the rough surface is observed for the Cassie's model. Nanostructure surfaces studied in this study can be explained by the Wenzel's model due to its hydrophilicity with a contact angle ranges from 0 to 45°. The Wenzel's equation can be completed by modifying the Young's equation which describes the plain surface, combining the roughness parameter ($\cos \theta_R = r \cos \theta$), where θ is the contact angle for the flat surface. Since the roughness(r), which is defined by the ratio of the actual solid surface area per unit of area projected on a horizontal plane, is greater than one, $\cos \theta_R$ is always greater than $\cos \theta$, which indicates that θ_R is lower than θ. Therefore, contact angle on rough surface is smaller than that on a polished surface of the same material.

Contact angle of the ZnO nanostructured surface was observed as 0°, completely wettable on the surface whereas contact angle of bare aluminum was measured about 96° as displayed in Figure 2.4 Contact angle measurement of bare aluminum (upper) and super-hydrophilic ZnO nanostructured surface (lower).As soon as drop was placed on the surface, the drop spread across the surface, which made it impossible to measure contact angle.

The surface roughness can provide the insight to evaluate possible bubble nucleation sites. Surface roughness of the surface was analyzed using Atomic Force Microscopy (AFM). The AFM image is shown in Figure 1.1Figure 2.5, indicating the average surface roughness is around 5863.2nm. Considering the average surface roughness of the polished bare substrate (31.54nm), the change of roughness is very significant.
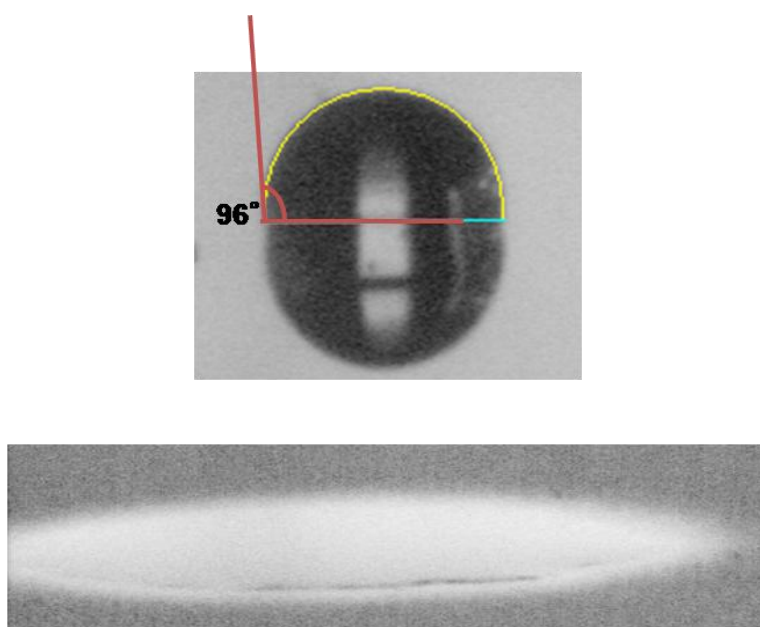
Figure 2.4 Contact angle measurement of bare aluminum (upper) and super-hydrophilic ZnO nanostructured surface (lower).
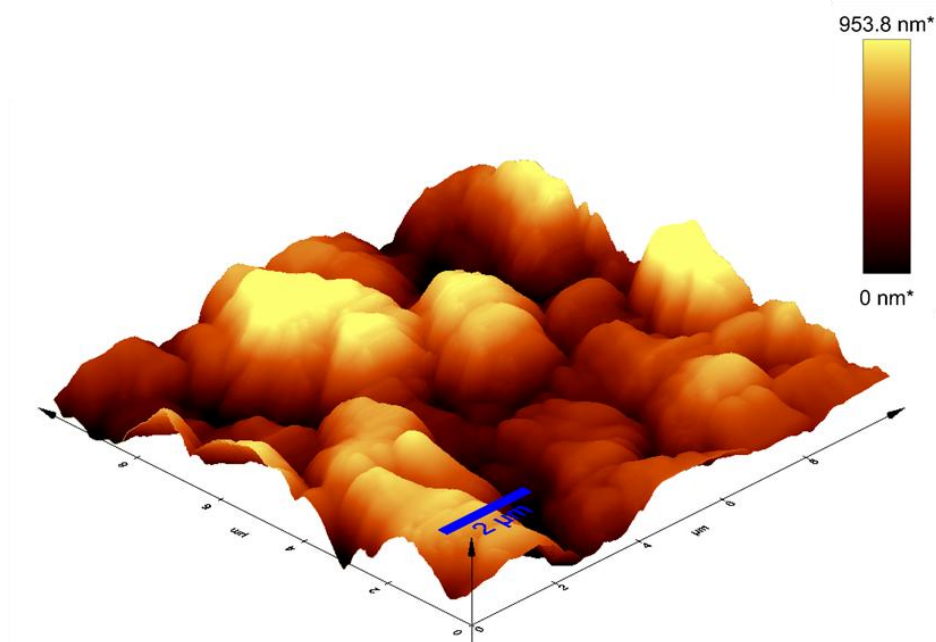
Figure 2.5 AFM image of super-hydrophilic ZnO nanostructured surface.

2.3.2 Hydrophilic ZnO nanostructured surface on aluminum

Hydrophilic ZnO nanostructured surface was also obtained by the MAND process using a different operating process parameter. A much lower NaOH concentration (0.01M) was used to prepare hydrophilic ZnO nanostructured surface, which is the only different process parameter from the process used for the preparation of super-hydrophilic ZnO nanostructured surface. According to the contact angle measurement, the surface is hydrophilic (44.8°) as displayed in Figure 2.6. Unlike the super-hydrophilic ZnO surface that is composing numerous pores, the hydrophilic surface morphology appears relatively smooth and contains much fewer pores as shown in Figure 2.7. Average surface roughness was evaluated to be around 79.6 nm, confirming that the surface is smoother with much less pores.

Figure 2.6 Contact angle measurement of hydrophilic ZnO nanostructured surface.
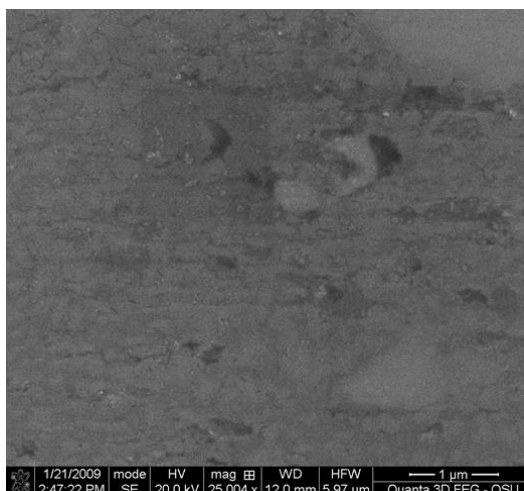
Figure 2.7 SEM image of hydrophilic ZnO nanostructured surface.

2.3.3 Flower like ZnO nanostrucured surface on aluminum

Flower like ZnO nanostructured surface were obtained by the MAND process on the aluminum substrates with high uniformity after carefully tuning the process parameters. As presented in Figure 2.8, flower like ZnO nanostructures cover almost the entire area of the substrate, embracing a great deal of various sized pores. Pore sizes of the flower like ZnO nanostructured surface are estimated to be around 50-

100nm, and pore densities are around 30-100/μm^2, determined by analyzing the SEM images. It is anticipated that more bubble nucleation sites can be enacted via cavities formed form the the petal of the flowers,. The flower like ZnO nanostructured surface was fabricated at a process condition in which 0.05M NaOH was used to adjust pH level, a substrate temperature of 250 ^{o}C , and a rotating speed of 2500 rpm.. The summary of MAND process parameters is in . In order to characterize the surface, both contact angle measurement and average surface roughness were performed and displayed in Figure 2.9and Figure 2.10 respectively. Consistent with Wenzel's model, the contact angle decreases with the increase of the surface roughness compared to the bare substrate. Contact angle value is 20° which shows a high wettability on the surface. The surface is also very rough according to an average surface roughness around 162.29nm determined by the AFM.

Table 2. MAND process parameters for flower like ZnO nanostructured surface

Type of ZnO surface	Concentration of NaOH (M)	Water bath temperature (°C)	Substrate holder temperature (°C)	Deposition time (min)	Rotating speed (rpm)	Flow rate (ml/min)
Flower like ZnO	0.05	70	250	10	2500	8.28

Figure 2.8 SEM images of flower like ZnO nanostructured surface in different
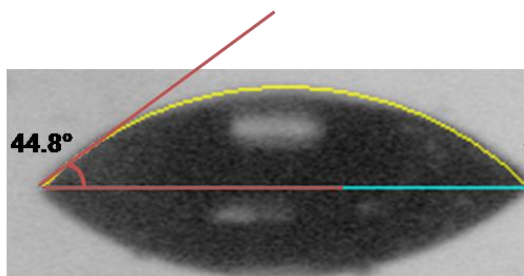
magnifications.

Figure 2.9 Contact angle measurement of flower like ZnO nanostructured surface.
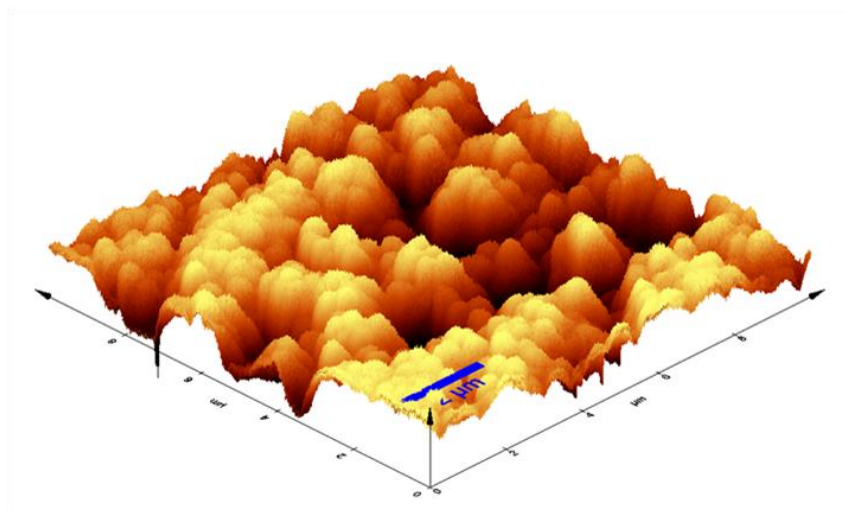
Figure 2.10 AFM image of flower like ZnO nanostructured surface.

2.3.4 Unique ZnO nanostrucured surface on aluminum

An unique ZnO nanostructured surface was prepared via the addition of a seed layer along with the MAND process. ZnO seed layer was first coated on the bare aluminum before the ZnO nanostructures were deposited using the MAND process. Most of MAND process parameters were similar to those used for the preparation of flower like ZnO, except a NaOH concentration of 0.10 M was used. The SEM image of the surface shown in Figure 2.11indicates that the morphology of the surface consists of finger-shaped nanostructures which are sitting on small sized flower like nanostructures. The contact angle of the surface at 18° is similar to the one of flower like ZnO surface at 20° as shown in Figure 2.12. The result of average surface roughness also demonstrates that the unique surface shows some similarities with the flower like surface in terms of surface morphology. The average surface roughness of the surface is around 258.03nm (Figure 2.13).
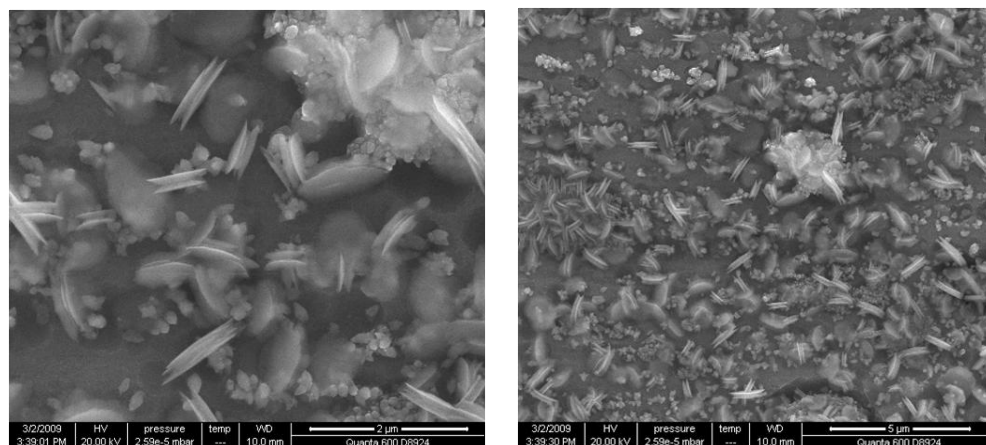
Figure 2.11 SEM image of unique ZnO nanostructured surface in different

magnifications.
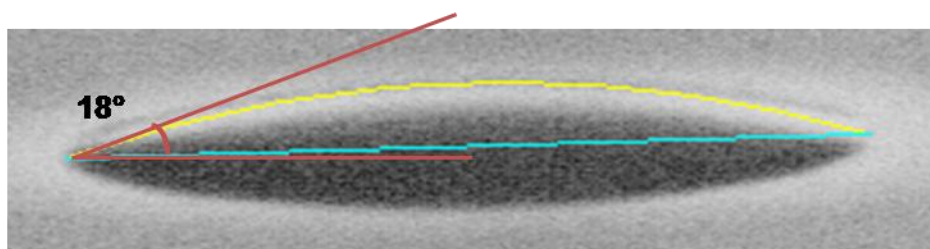
Figure 2.12 Contact angle measurement of unique ZnO nanostructured surface.
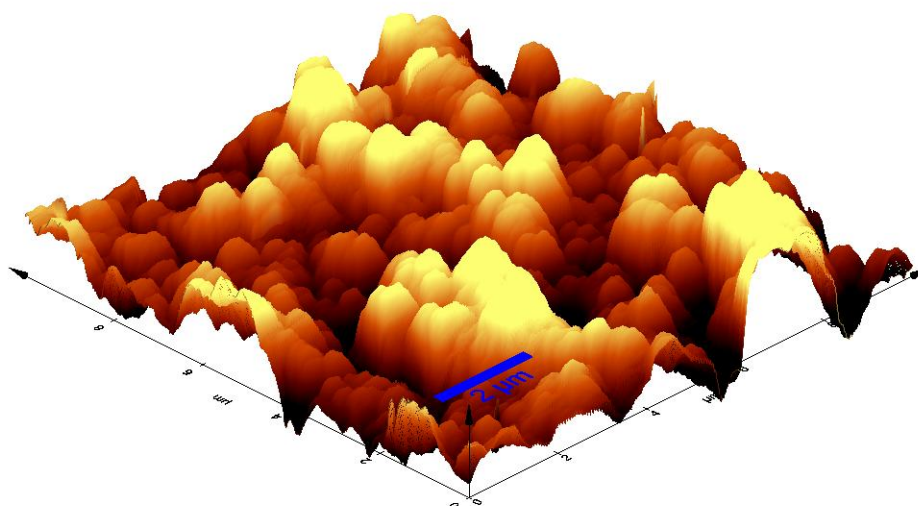
Figure 2.13 AFM image of unique ZnO nanostructured surface.

2.3.5 Flower like ZnO nanostrucured surface on copper

Flower like ZnO nanostructured surface was also fabricated on the copper substrate using the MAND process. While various types of ZnO morphologies can be fabricated on the aluminum substrates by varying the MAND process parameters as discussed in the previous sections, only flower like ZnO nanostructured surface was obtained on the copper substrates regardless of parameter changes. The morphology presented in Figure 2.14was obtained in the same process parameters that were applied to prepare the flower like surface on aluminum. Similar with the flower surface on aluminum, individual flower is made by some petals which are grown vertically. The coverage of ZnO nanoparticles on copper was not as good as those were deposited on the aluminum substrates. This could be a cause of lower wettability of the copper substrate, indicating that contact angle is 39.7° compared that of 20° was measured for

flower like structures on aluminum (Figure 2.14). Average surface roughness of the surface is around 183.637 nm as shown in Figure 2.16.
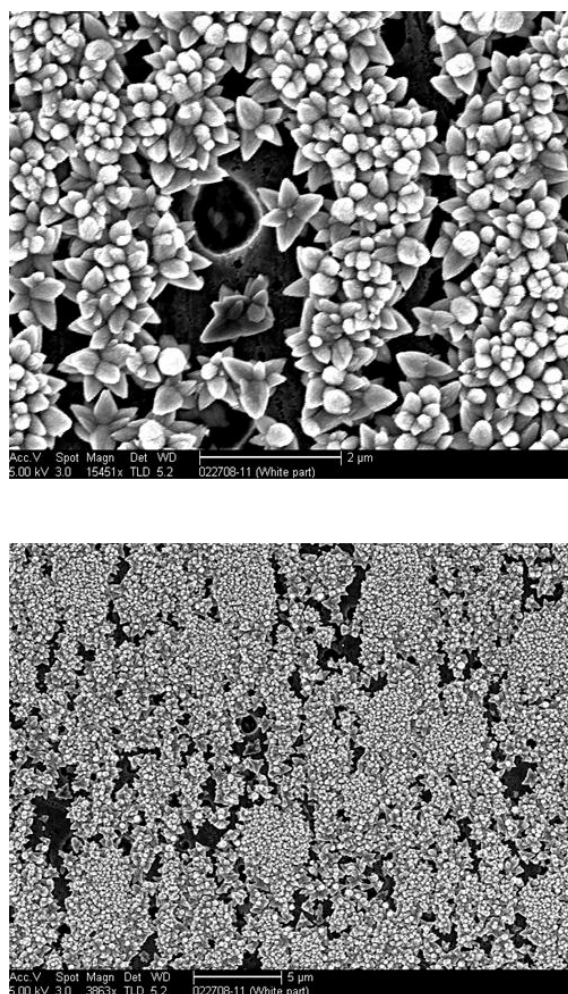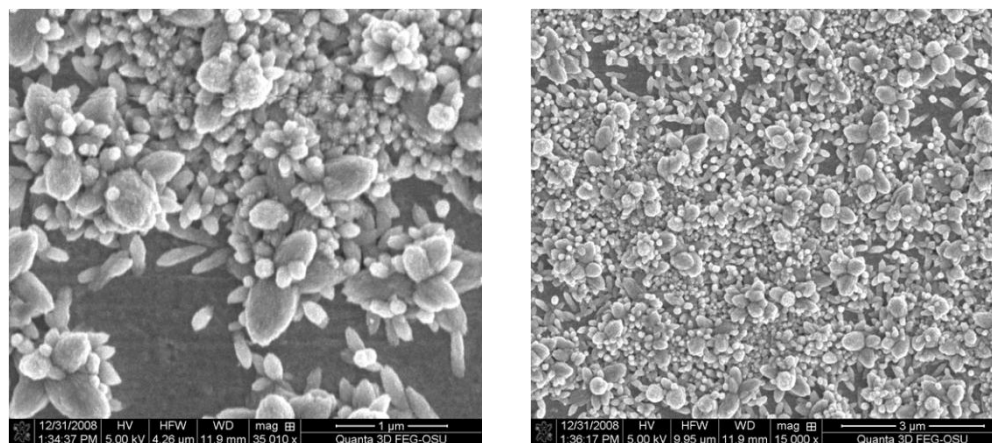

Figure 2.14 SEM images of flower like ZnO nanostructured surface on copper in different magnifications.
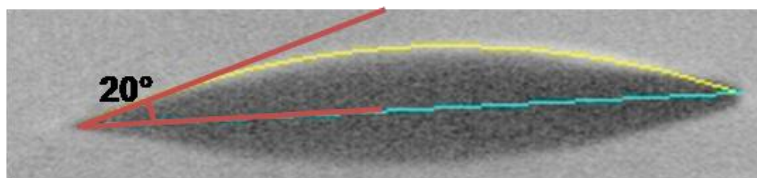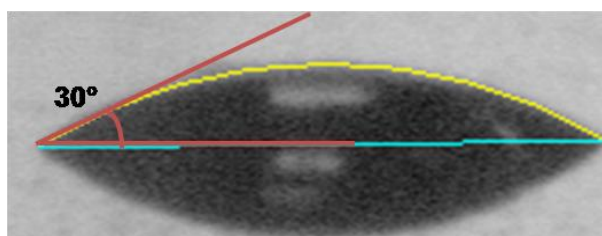

Figure 2.15 Contact angle measurement of flower like ZnO nanostructured surface on copper
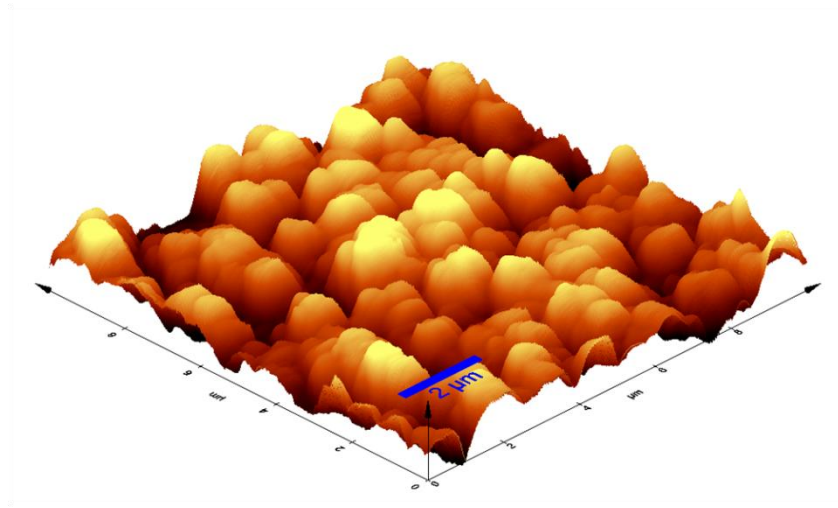
Figure 2.16 AFM image of flower like ZnO nanostructured surface on copper

For the application of pool boiling, a total of five different ZnO nanostructured surfaces were fabricated and characterized to evaluate their properties. The results of both contact angle and average surface roughness are tabulated for a quick comparison as given in Table 2.1.

Table 2.1 Characteristic summary of ZnO nanostructured surfaces

Type of ZnO surface	Contact angle (°)	Average surface roughness (nm)
Super-hydrophilic	0	5863.2
Hydrophilic	44.8	79.6
Flower like surface	20	162.29
Unique surface	18	258.03
Flower like on Cu	30	183.64

2.3.6 ZSM-5 zeolite on silicon

Characterization of ZSM-5 zeolite, which was synthesized by hydrothermal reaction, was also performed. SEM image of the zeolite is presented in Figure 2.17. A number of micron sized rod shaped zeolite completely covers entire area of the substrate. Irregularly growing zeolite can create micron sized pores formed between zeolite rods. The wettability of the zeolite surface was evaluated by contact angle measurement as shown in Figure 2.18. The zeolite surface has good agreement with Wenzel's model, presenting 14°. X-ray Diffraction (XRD) pattern of the zeolite surface is also analyzed in Figure 2.19, indicating that only b-oriented film was obtained according to the XRD data.
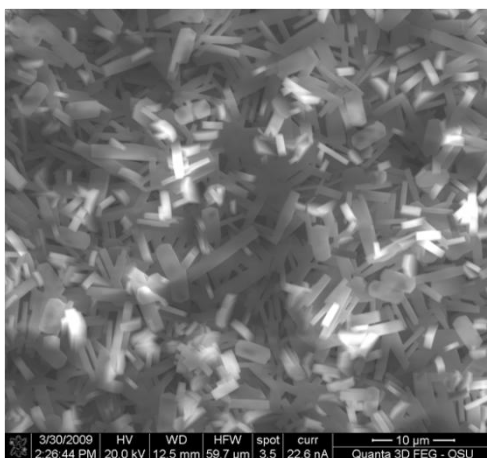
Figure 2.17 SEM image of zeolite structure.
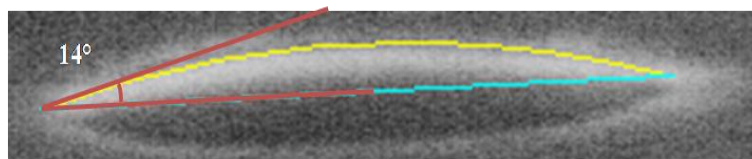
Figure 2.18 Contact angle measurement of zeolite surface.
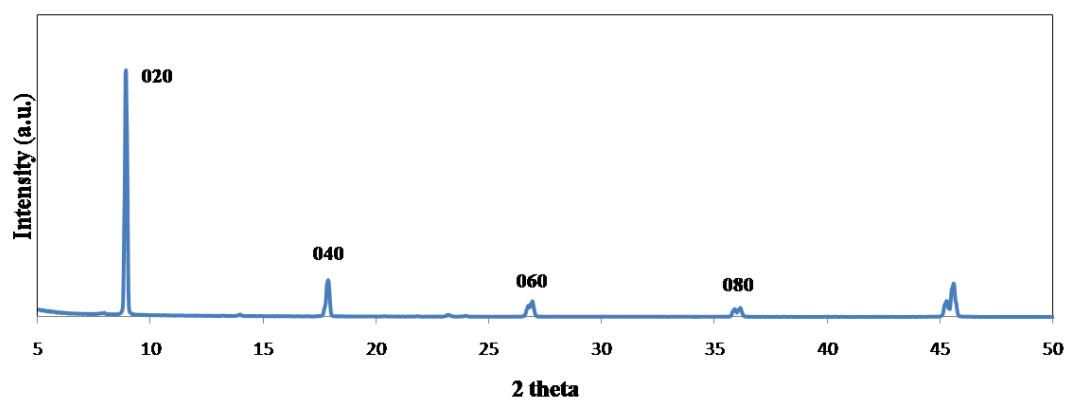
Figure 2.19 XRD pattern of zeolite surface.

3   Pool boiling performance

3.1   Pool boiling experiment facility and procedure

The schematic illustration for the pool boiling experiment is shown in Figure 3.1. The boiling test facility consists of copper heating block, electrical resistive heaters, and boiling chamber which is made from polycarbonate material. Heat was supplied through four 50Ω resistors soldered under the copper heating block to provide the uniform heat distribution on the copper block. Boiling surface coated with ZnO nanoparticles was mounted on the copper heating block by soldering. Twelve K-type thermocouples were implemented to measure temperature. Two thermocouples were immersed in the boiling chamber to evaluate water temperature. In order to measure boiling surface temperature, two thermocouples were bonded on the surface using thermal epoxy. Temperature gradient in the copper block was also measured by implementing two differential temperature thermocouples. Temperature of the heater was read by thermocouples attached to the heaters. The boiling test facility was completely insulated by fiber glass material to assure as close as possible to one-dimensional heat flux toward the boiling surface, and the boiling chamber is also insulated by the same insulator to minimize the heat loss. The uncertainty of the measurement was estimated to be less than ± 10.2%. A CCD camera was employed to capture the visual images of boiling performance. Data acquisition system incorporated with LABVIEW program continuously monitored and recorded all of the
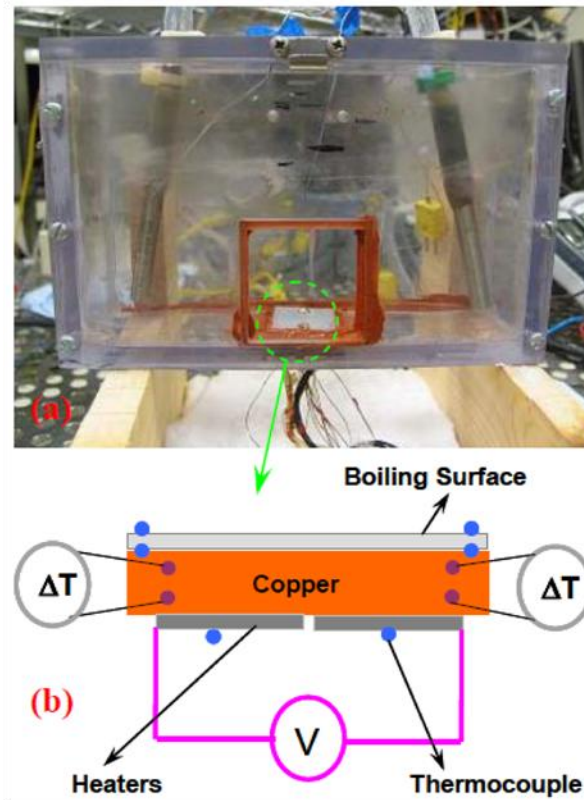
Figure 3.1 Schematic illustration of the instrumented test heater assembly.

electrical input values as well as temperature readings. The experiment was performed

at atmospheric pressure. Prior to performing the boiling test, a degassing process of DI

water was rigorously carried out to assure the removal of dissolved gas for one hour

using two cartridge heaters immersed in the boiling chamber. DI water was used

throughout the whole experiment. Once the DI water in the boiling chamber reached

saturation temperature (100°C), the cartridge heaters were gradually turned off

ensuring it continuously stayed at 100°C during the boiling test. After maintaining

saturation temperature, the power on the copper heating block assembly was turned on.

At the beginning of the boiling test, the increment of heat flux was kept about 5W/cm^2.

However, as CHF was approaching, the increment of heat flux was reduced to $2W/cm^2$ in order to obtain more accurate CHF value. At the incipience of CHF, the heater temperature rapidly jumped up, which could cause the electrical heater to burn out, so the power was removed immediately to avoid the damage to the heater. The boiling performance was repeated with selected surfaces to assure the credibility of the test result.

3.2   Pool boiling test results and discussion

3.2.1 Pool boiling performance of the ZnO nanostructured surfaces

Pool boiling experiment was performed following the process described in previous section with the nanostructured surfaces which were characterized. CHF data of the ZnO nanostructured surfaces investigated in this study are compared in Figure 3.2. The boiling curves of all the surfaces shows a good agreement with those which were published by other researchers. Since bubble nucleation and growth regimes are only within our interest, pool boiling experiment has been conducted before reaching transition boiling regime.

Boiling test with bare aluminum was primarily performed as a reference. The CHF of bare aluminum was observed about 23 W/cm^2. As indicated in Figure 3.2, superheat was surged when CHF was observed. In fact, the burning out of heaters attached beyond heating block occurred in the presence of CHF.
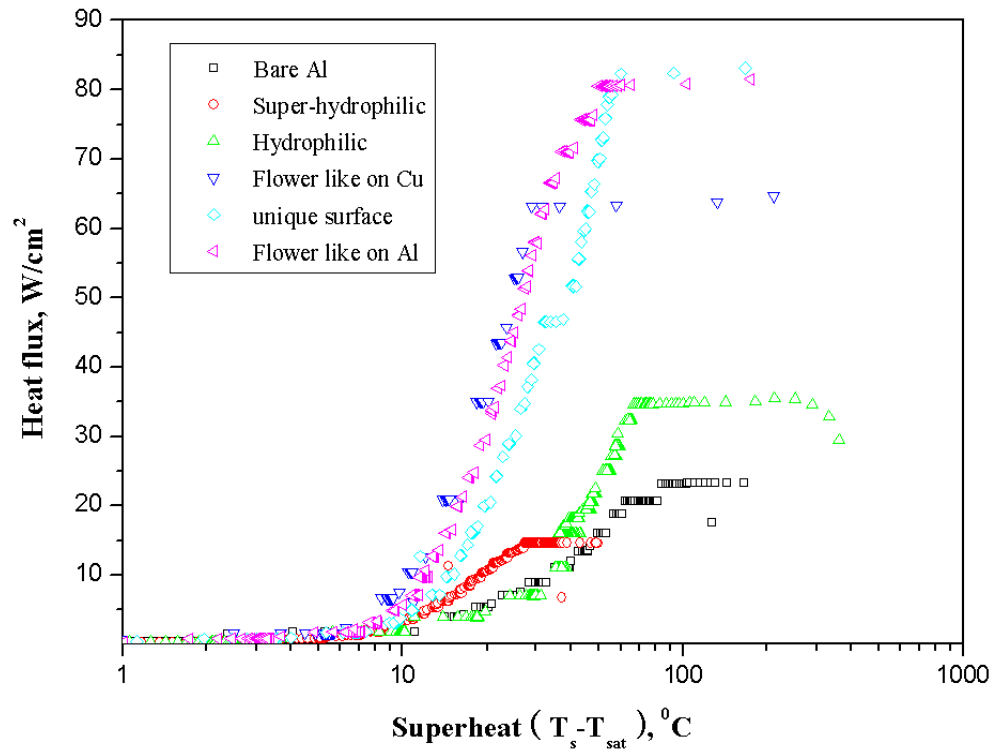
Figure 3.2 Pool boiling curves for the ZnO nanostructured surfaces.

Pool boiling for super-hydrophilic surface was performed and it was observed that the CHF of the surface is lower than the one for bare aluminum, showing about 15 W/cm^2. This is contrary to some of the reported pool boiling data that were conducted on surfaces that are very rough as well as good wettability [6, 7]. However, in this pool boiling test opposite result was observed, which can compromise the relation of surface wettability and roughness for enhanced heat transfer surface. In fact, the roughness itself only could not explain the improvement of heat transfer performance although it is closely associated with the number of bubble nucleation sites. A rough

surface is more likely to have more cavities. As shown in the SEM and AFM images, the super-hydrophilic surface is very rough and contains a large number of pores. More detailed examination of the surface morphology suggests that ZnO nanoparticles on the super-hydrophilic surface, forming pores on the surface, cannot make the complete cavities. In other words, the pores on the super-hydrophilic surfaces are more likely to become open pores rather than being typical cavities as described in Figure 3.3. In open pore system, fluid trapped into the pores tends to merge due to the surface tension, which can restrict the bubble growth and eventually make bubble release difficult in limited pore size

Another potential reason of being lower CHF is related to the wettability of the fluid on the surface. As shown in Figure 2.4, the contact angle of the surface is too small to measure. This indicates that fluid can completely wet the pores on the surface, leaving no vapor trapped in the cavities. The presence of trapped vapor plays a significant role in achieving bubble nucleation in lower superheat as confirmed by some experiments [30, 31].

The CHF values for the rest of the ZnO nanostructured surfaces are consistent with trend that has been characterized and demonstrated by other researchers. Hydrophilic ZnO surface having 45° contact angle showed higher CHF value than one for bare aluminum with 96° contact angle.

Typical cavity   Open pore for super-hydrophilic surface
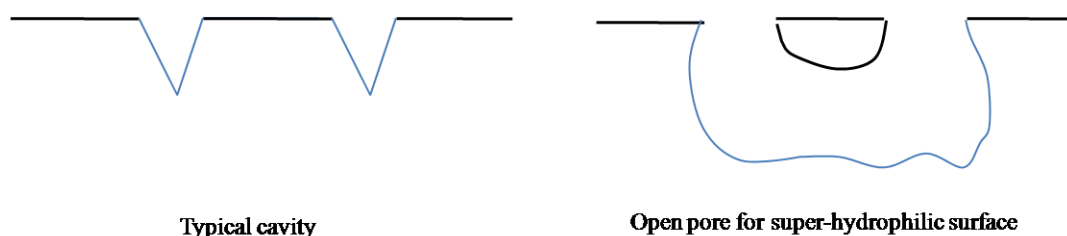
Figure 3.3 Comparison of typical cavity and open pore for super-hydrophilic surface.

For the unique ZnO surface, the CHF value reaches almost 82 W/cm^2 which is the second highest among the surfaces studied in this research. It is hypothesized for the significant enhancement of the CHF value that finger-shaped nanostructures, seemingly bended structure, can act like cavities providing the ability of trapping air efficiently and enact the bubble nucleation. The surface also possesses favorable condition for pool boiling performance in terms of good wettability of 18°, the lowest contact angle measurement in this research. Heat flux plateau is observed near 45 W/cm^2 heat flux with increase of superheat for the unique structure as shown in pool boiling curves (Figure 3.2). The heat flux plateau has been observed when bubble nucleation, which is requiring certain minimum superheat, is activated [32].

Pool boiling experiment for flower like ZnO nanostructured surfaces on aluminum and copper was also performed and CHF values are compared in Figure 3.2. It is observed that the CHF of the flower like nanostructured surface reach to 82.5 W/cm^2 while CHF of polished bare aluminum substrate is approximately placed on 23 W/cm^2. The boiling curve indicates that the CHF of the surface jumps to more than three times, compared to that of the bare aluminum substrate. This CHF enhancement

has also been consistent with previous boiling test results that have been reported by Bang et al. and Kim et al [6, 7]. They used nanofluids as a coolant to precipitate nanoparticles on the boiling surface during boiling performance. They also described the surface modification resulting from nanoparticle deposition is the main reason of the CHF enhancement providing more active sites for bubble nucleation. It is worth noting that the magnitude of the CHF increase in this boiling test is considerably greater than any other reported boiling tests. In fact, considering only the CHF increment, this result is one of the most enhanced CHF performances. The flower-like nanostructured surface provides more activated bubble nucleation sites due to its unique structure, creating numerous cavities. Pore sizes for the flower-like ZnO nanostructured surface are 50-100nm, and pore densities are 30-100/μm^2 as described in previous section. In addition, the petal orientation of the flower, growing vertically, is also favorable in leading to advanced heat transfer performance by making the bubble easily released from the surface, delaying the drying out caused by the thin vapor film formed between the boiling surface and the bulk coolant.

The photographs depicting the boiling performance for bare aluminum and flower like nanostructred surface are shown in Figure 3.5. It is apparent that more bubbles are activated on the nanostrucured surface than on the bare aluminum surface in the regime of bubble nucleation, leaving some empty space without activated bubbles on bare aluminum (a, b). The bubble phenomena at the CHF for both surfaces are also exhibited in Figure 3.5(c, d). The mushroom shape bubble columns, generally

shown near the CHF, were observed on both surfaces. The vapor film existing between the surface and the fluid was also observed near the CHF regime.

When it comes to contact angle measurement, the flower like nanostructured surface is very wettable allowing fluid to wet the surface favorably after constant bubble departure. Same reasoning is also implied for the flower like ZnO nanostrucured surface on copper substrate. Because of less wettability with 30° contact angle, it is considered that the CHF value for the surface on copper was placed about 64 W/cm^2.

The schematic diagram to describe the relation between surface characterizations and CHF improvement is shown in Figure 3.4 for comparison of the surfaces.
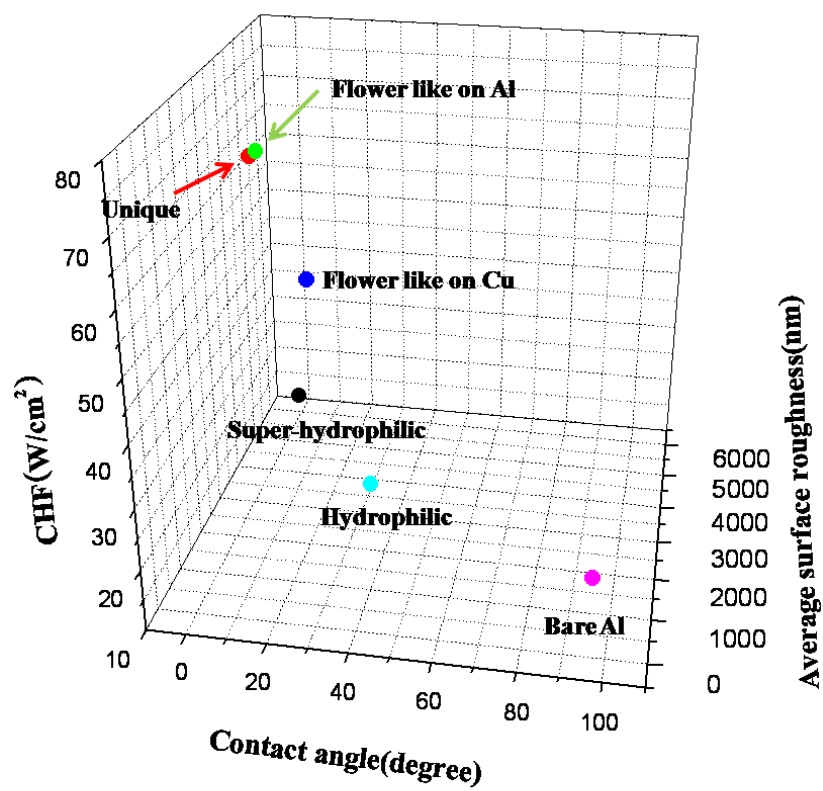
Figure 3.4 Correlation of surface characterization and CHF values.
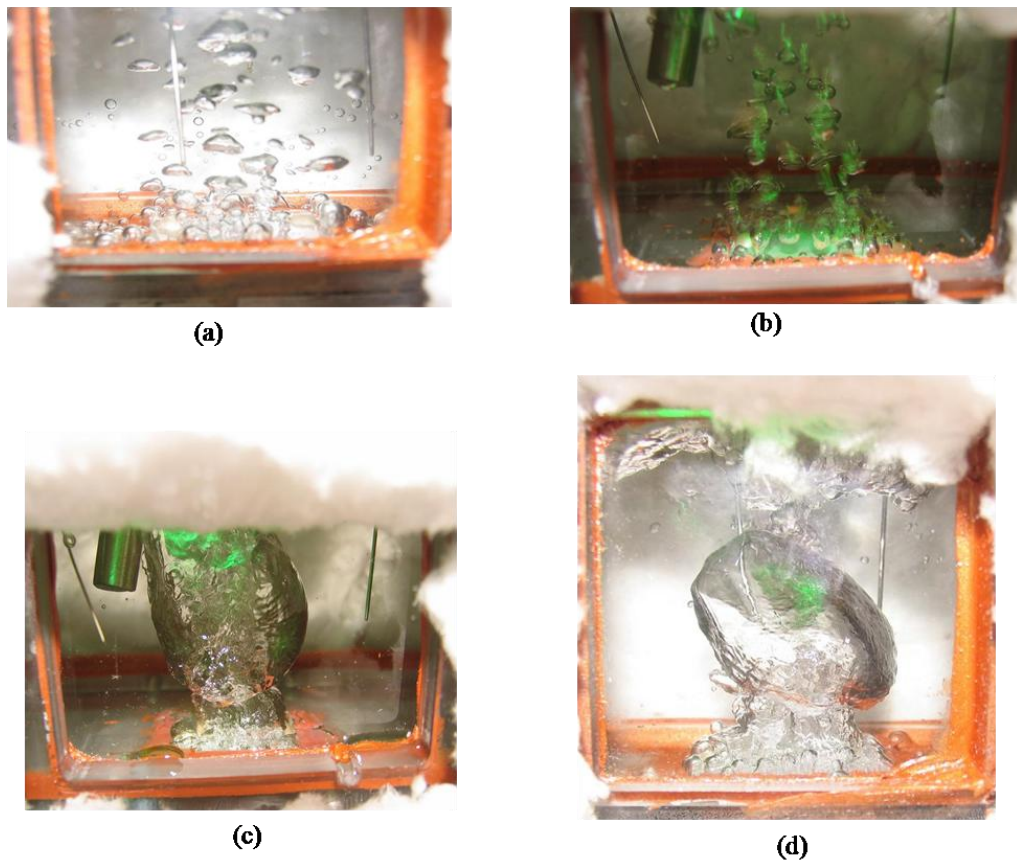
Figure 3.5 Photographs of pool boiling stage: (a) onset of bubble nucleation for bare aluminum and (b) for ZnO nanostructured surface, (c) CHF for bare aluminum, (d) and for ZnO nanostructured surface.

The plots of heat transfer coefficient (HTC) of ZnO nanostrucutured surfaces as a function of heat flux are provided in Figure 3.6. HTC can be achieved by dividing the heat flux by superheat. All the HTC data including from bare aluminum to flower like nanostructured surfaces are compared in Figure 3.6. The HTC of the super-hydrophilic surface is similar with the one for bare aluminum whereas the hydrophilic surface shows the increase of HTC at high heat flux. As predicted based on the CHF data, the ZnO nanostructured surfaces that are achieving significant CHF enhancement demonstrates that HTC is also highly improved regardless of the magnitude of heat flux. Especially for the flower like ZnO nanostructured surface on aluminum substrate, the HTC is about an order of magnitude higher than that of bare aluminum in the nucleate boiling regime. These results are contrary to the result reported by Bang at el. who observed that HTC is decreased with increase of the CHF [6]. Some of the researchers, however, have reported that HTC is also enhanced along with the increase of CHF using various nanostructured surfaces like CNT and nanowires [8, 33].
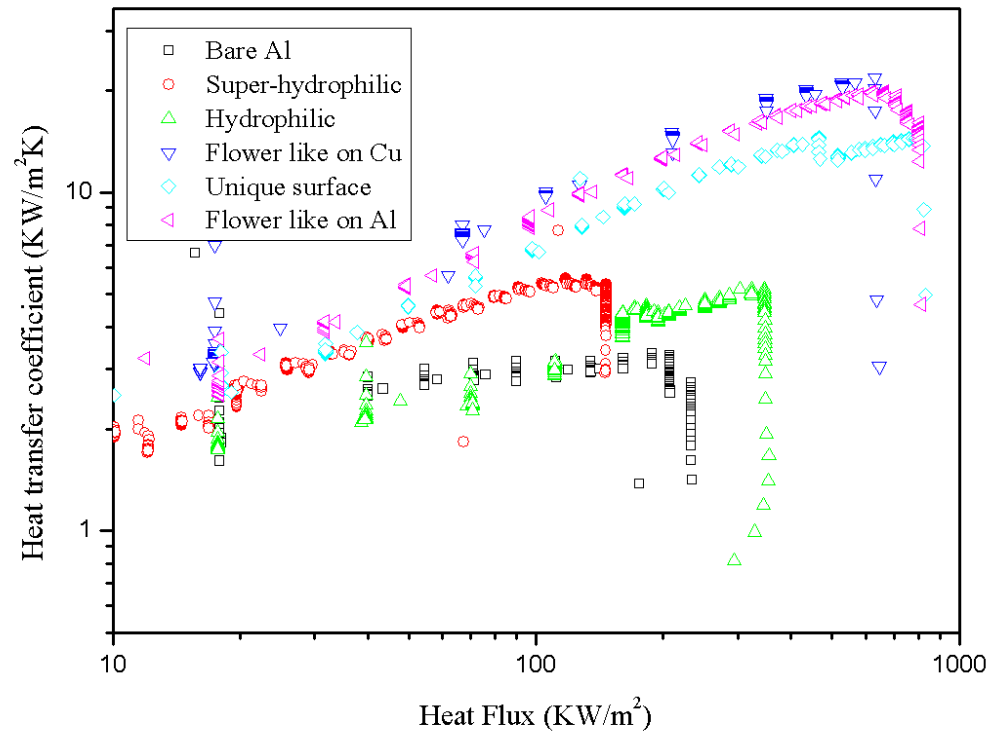
Figure 3.6 Heat transfer coefficient of ZnO nanostructured surface as a function of

heat flux (log-log plot).
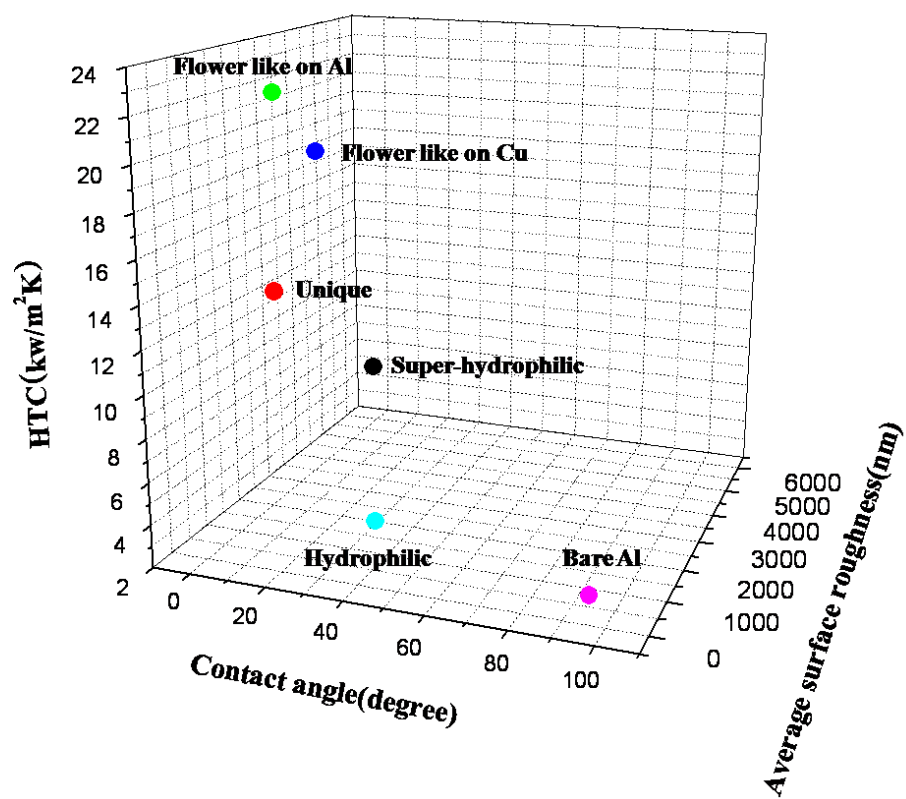
Figure 3.7 Correlation of surface characterization and HTC values.

3.2.2 Pool boiling performance of the ZSM-5 zeolite surface

ZSM-5 zeolite was used to investigate the pool boiling heat transfer. The CHF of the zeolite surface is presented in Figure 3.8. Pool boiling for pure silicon substrate was performed for the comparison of CHF to the zeolite surface. The CHF value of the pure silicon is about 32 W/cm^2. It is apparent according to the CHF data that the zeolite surface has some heat flux plateaus as shown in the unique ZnO surface. In addition, the improvement of the heat flux of the surface is very small while the increase of superheat is rapidly soaring. Burning out of the heaters that are bonded below the zeolite surface occurred in the lower heat flux, compared to other ZnO nanostructured surfaces investigated in this study. The CHF value was not obtained during pool boiling performance due to the repeated heat flux plateau. As explained in the unique ZnO surface, bubble nucleation on the zeolite surface is very limited in lower superheat, and as approaching certain superheat more cavities could be enacted. This phenomenon had been repeated during pool boiling experiment, which eventually resulted in some heat flux plateaus. A hypothesis can be proposed in order to understand this pool boiling result. The general pore size of ZSM- 5 zeolite has been reported around 6 Å. The bubble growth and bubble escape from the cavity can be restricted in such a small cavity radius, resulting in the bubble to remain into the cavity for long period of time. Although the zeolite is very wettable with 14° contact angle due to the strong hydrophilicy of the zeolite framework, the significant defect on the cavity radius size offsets the effect of the wettability. This reasoning is supported

by classical theories that nanometer-scale pores are considered too small to set the bubble to grow and release [34, 35].

HTC data as a function of heat flux is presented in Figure 3.9. Since pool boiling curve of the zeolite surface shift from left to right compared to one for the pure silicon substrate, it is predicted that HTC values of the zeolite surface would placed below those for the pure silicon substrate. Indeed, HTC data of the zeolite surface in Figure 3.9 confirms that pure silicon substrate is more favorable than the zeolite surface in terms of more efficient heat transfer.

Figure 3.8 Pool boiling curves for ZSM-5 zeolite surface.
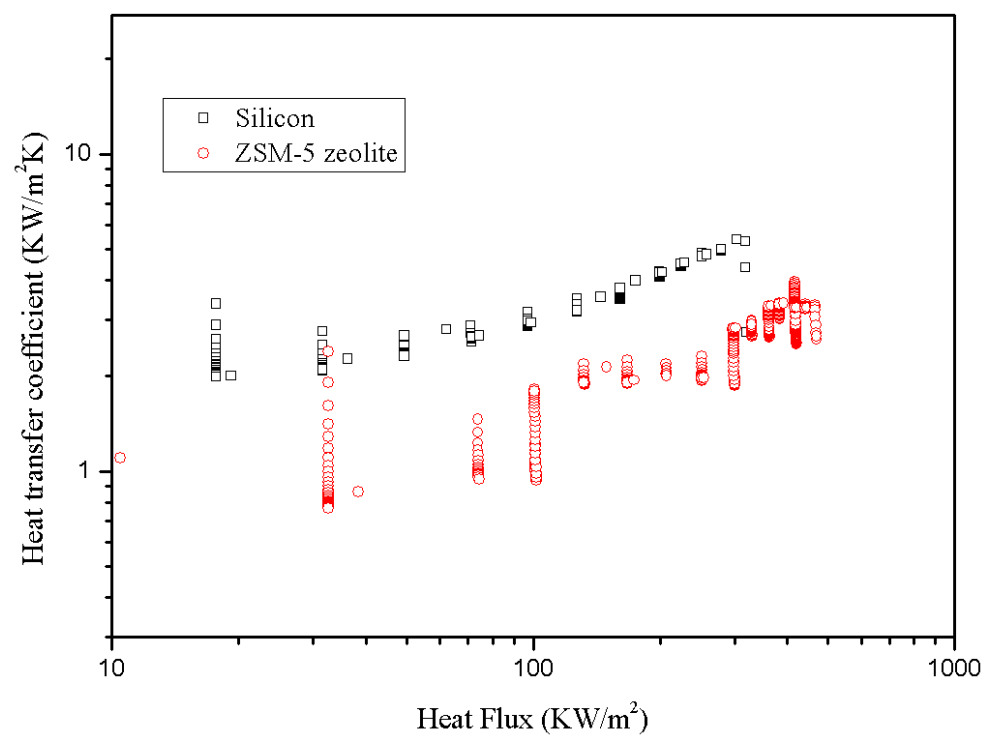
Figure 3.9 Heat transfer coefficient of ZSM-5 zeolite as a function of heat flux (log-

log plot).

4   ZnO nanoparticle deposition in minichannel for convective flow boiling
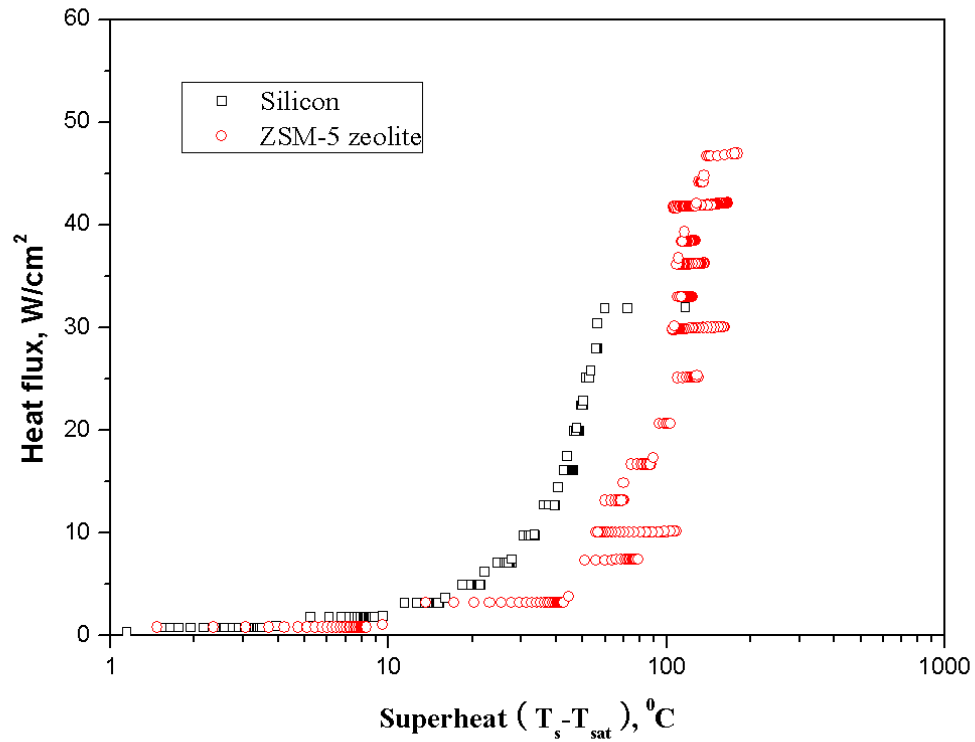
Different shapes of ZnO nanostructured surfaces which supposedly impact the heat transfer performance were coated on the bottom of minichannel heat sink consisting of seven parallel channels with hydraulic diameter of 600 μm. It was demonstrated for our past pool boiling experiment that ZnO nanostructured surfaces prepared by MAND^{TM} method showed various morphologies in the change of process parameters and led to the significantly enhanced heat transfer performance in both CHF and heat transfer coefficient (HTC). Most of the ZnO nanostructured surfaces coated on aluminum or copper polished substrate possessed the highly wettable property as well as the great extent of roughness. Two different ZnO nanosturctured surfaces for flow boiling experiment were obtained using flow cell which was made by modification of MAND. Design modification of the original MAND which is particularly designed for nanoparticle deposition on a polished substrate was achieved by replacing stainless steel plate with a flow cell in order for the deposition on the bottom of minichannel. The ZnO nanostructured surfaces evaluated for the flow boiling test were characterized by SEM and XRD analysis.

4.1   Deposition of ZnO nanoparticles in minichannel heat sink

Experimental facility for the fabrication of ZnO nanoparticles in minichannel consists of a microprocessor controlled dispensing pump (Ismatec micropumps), a 1.22 mm ID Tygon ST tubing (Upchurch Scientific), a T-mixer (Upchurch scientific), and flow cell where minichannel was placed. Minichannel was adhered to the flow cell with thermal paste (Arctic Silver). The flow cell which is made by copper material

was designed for uniform heat distribution throughout the minichannel. Desired

amount of heat was supplied by six cartridge heaters which are embedded inside the

flow cell. The temperature readings of the flow cell were continuously monitored by

two k-type thermocouples placed on the top of flow cell and interpreted via

LABVIEW software. The flow cell was completely insulated by insulator material.

The cover made from polycarbonate material was set on the flow cell, so the

deposition process can be observed visually. The schematic diagram of continuous

micro reactor facility including the image of the flow cell is shown in Figure 4.1. In

this experiment, the reactant streams, A and B, were initially pumped into the Tygon

tube and allowed to mix in the T-mixer. Stream A consisted of 0.005M aqueous zinc

acetate solution and 0.25M aqueous ammonium acetate solution. Stream B consisited

of 0.05M aqueous solution of sodium hydroxide. The solution mixture of A and B was

passed through a 5ft long Tygon tube immersed in a water bath maintained at constant

temperature. The solution then entered to the flow cell maintained at constant

temperature through an inlet port and flowed into the minichannel which is placed on

the notch of the flow cell. ZnO nanoparticles were deposited as the solution passed

through the minichannel, following a thin film growth mechanism based on

nanoparticles formation and sticking. The solution then flowed out through an outlet

port.
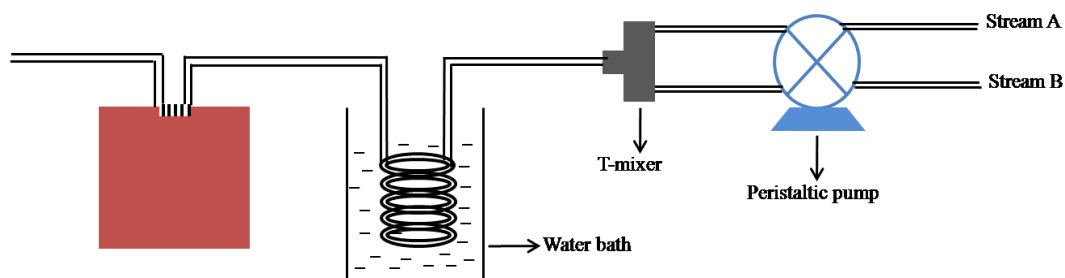
Figure 4.1 Schematic diagram of continuous micro reactor facility and the image of

the flow cell.

4.2   Understanding of the flow distribution

Prior to conducting the ZnO nanoparticles deposition in the minichannel heat

sink, the investigation of the flow distribution in minichannel was conducted. The

flow distribution in minichannel plays a significant role in determining the uniform

ZnO nanostructured film deposition along the minichannel from inlet to outlet as well

as the uniform deposition on individual minichannel. An investigation regarding the

flow distribution in microchannel was performed by Suresh V. et al. [36]. They

exploited the flow distribution with both experimental and numerical solutions and also showed the importance of manifold shape of the flow cell, describing that rectangular design manifold yielded a significantly lower flow maldistribution compared to recessed shaped manifold. Referring to this investigation, rectangular design manifold was employed and the simulation using COMSOL software was also carried out to determine an optimum flow rate for uniform flow distribution, which eventually results in uniform ZnO nanoparticle deposition along minichannel. The computational solution that was implemented for the flower like ZnO nanostructured surface is presented in Figure 4.2. For the simplification of the computational solution, some assumptions were made: steady state, laminar flow, constant fluid property, and incompressible fluid. Both Navier-Stokes equations and continuity equation were applied along with reasonable boundary conditions. Due to the symmetry structure of minichannel heat sink, half of the heat sink was studied and no convective flux was implemented across the symmetry plane. No slip boundary condition was applied at the wall of each channel. Appropriate velocity that is corresponding to the volume flow rate of the mixed solution was also implemented for the numerical analysis. It is apparent according to the simulated analysis that the critical maldistribution in minichannel was not observed, supplying uniform flow distribution in all of the channels as shown in Figure 33. Velocity magnitude and streamline across the flow cell including minichannel are also presented in Figure 4.2.
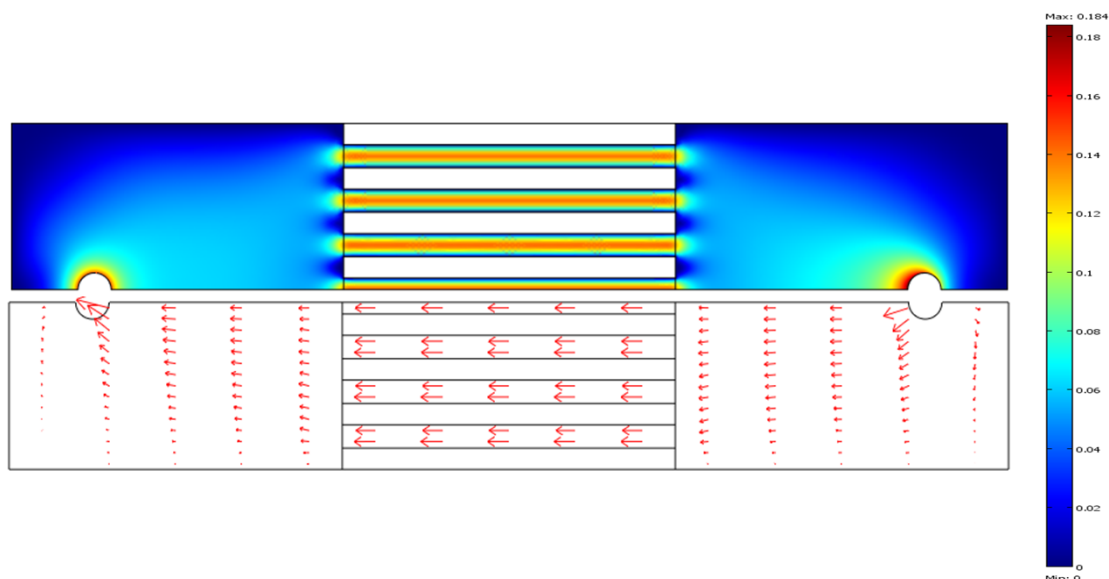
Figure 4.2 Velocity magnitude and streamline evaluated by the analytical study in

minichannel.

4.3   Characterization and discussion of ZnO nanostructures in minichannel

SEM images of two different ZnO nanostructured surfaces are presented in Figure 4.3. The unique ZnO nanostructured surface was observed as shown in Figure 4.3 (a) and (b), which exhibit low and high magnification respectively. This morphology is similar with the nanostack structure reported by Changhui YE [23]. According to the SEM images, small size of nanostructures (~1nm), finger like shape, are randomly scattered on the nanoflake structure with high density. The uniformity of this structure is consistent regardless of the location of minichannel. This morphology was fabricated in relatively low NaOH concentration (0.05M), which is corresponding to pH 9~10, compared to that for flower like structure. It has been reported that the

nanoflakes ZnO structures have generally appeared on low pH level, compared to other ZnO nanostructures such as nanoprisms and flower like structures [27]. This unique structure consisting of the combination of finger like structure and nanoflakes was demonstrated in term of the significantly enhanced CHF as well as HTC in the past pool boiling test.

The second ZnO nanostructured surface described in this study is flower like nanostructure as displayed in Figure 4.3(c) and (d). While the unique ZnO nanostructured surface is consistent in terms of the nanostructure density throughout the minichannel, the flower like ZnO nanostructured surface showed variations along the minichannel.
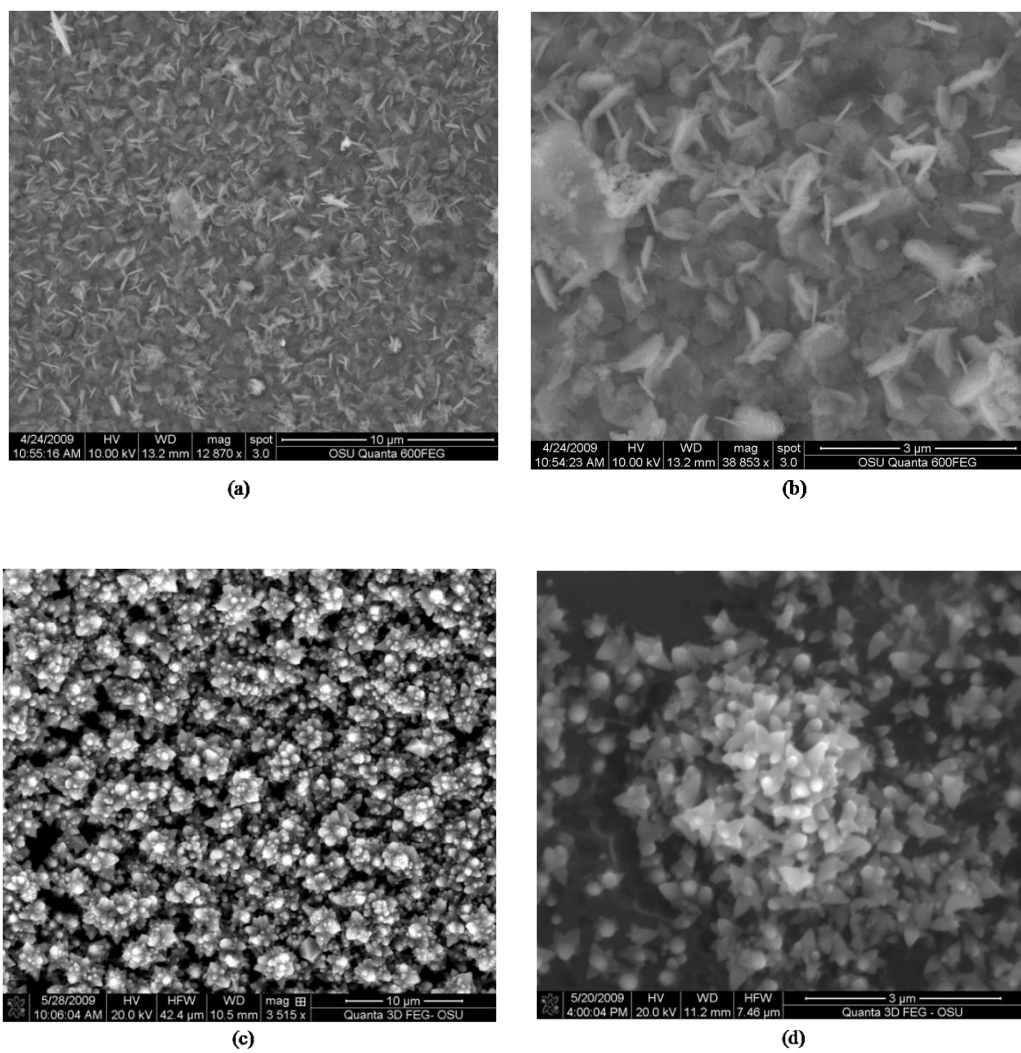
Figure 4.3 SEM images of ZnO nanostructures in minichannel: (a), (b) unique strutures and (c), (d) flower like structures.

We hypothesized the major factor causing these varied uniformities is either that maldistribution occured during ZnO nanoparticle depostion or that temperature distribution was not even throughout the bottom of minichannel. Some of assumptions made for the simplification of the simulated flow distribution study could not be valid in real deposition process. For instance, the solution passing through minichannel was considered homogeneous solution in the computational analysis. However, it actually contained some aggregated ZnO nanoparticles which were built by Oswald's ripening (OR) mechanism and suspiciously interfere with the flow pattern of the solution in the Tygon tube and minichannel, which can lead to maldistribution. Considering the comparison of NaOH concentration implemented for two ZnO nanostructured surfaces, the flower like ZnO structure is more likely to cause maldistribution than unique structure. This is due to the fact that the quantity of OH^- ion for the flower like surface is more than one for the unique structure and more ZnO nanoparticles are created in the higher presence of the OH^- ion.

The flower like ZnO nanoparticle surface was synthesized under high NaOH concentration (pH 12~13), which is consistent with the explanation reported by D. Vernardou et al.[27]. Hahn et al also vindicated the role of NaOH concentration, proposing growth mechanism of flower like ZnO nanostructures [24]. The process parameters for the synthesis of two ZnO nanostructures are summarized in table 4. It is worth noting that different flow rate was applied for obtaining ZnO nanostructured surfaces, which resulted in different residence time. One of the major parameters in

Table 4.1 Comparsion of process parameters for unique and flower like structures

ZnO structure	Concentration of NaOH (M)	Water bath temperature (°C)	Flow cell temperature (°C)	Deposition time (min)	Flow rate (ml/min)
Unique structure	0.05	60	40	10	5
Flower like structure	0.10	60	40	10	10

determining the morphology of ZnO nanostructured surface could be the residence time along with the NaOH concentration because the growth of ZnO nanoparticles is affected by residence time. The residence time was simply controlled by adjusting the flow rate of two streams in this continuous process because the length and diameter of the tube used for deposition process were constant through the whole experiment. The residence time for obtaining the unique surface was around 12 second whereas 6 second for the flower like ZnO nanostructure. The phase of ZnO nanostructured surfaces was characterized by XRD. XRD pattern of the unique ZnO nanostructure and flower like ZnO nanostructure are shown in Figure 4.4 (a) and (b) respectively. XRD data reveals the standard pure ZnO phase with hexagonal wurtzite structure in which peaks are presented at 32° (100), 34° (002), and 36° (101). Four strong peaks from 40° to 80° are result of aluminum substrates. The peaks for ZnO phase are magnified and displayed in the inset. The unique ZnO nanostructured surface has a poor crystal quality, presenting low and equivalent intensity. On the other hand, the flower like surface has a preferred orientation (002) which is almost three times stronger than two other peaks (100) (101).

Further research should be conducted in order to elucidate the ZnO growth mechanism in the continuous flow minichannel.
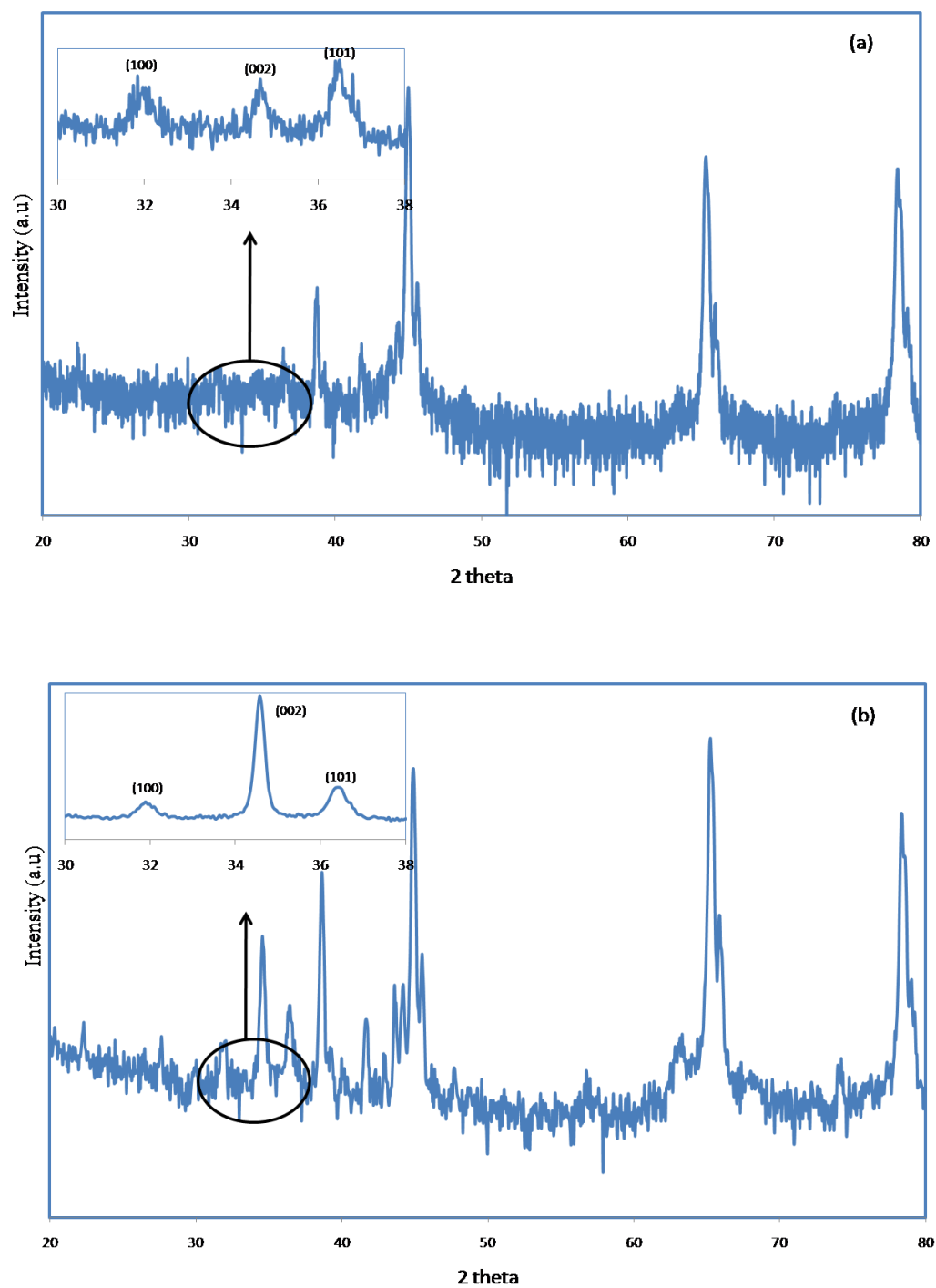
Figure 4.4 XRD patterns of (a) unique ZnO structure and (b) flower like ZnO structure.

5   Conclusion and future work

Nanostructured surfaces, which are including various ZnO morphologies and ZSM-5 zeolite, were fabricated on various substrates. The deposition of two different types of ZnO nanostructures in the minichannel was also performed using the flow cell. These surfaces were characterized by SEM, AFM, and contact angle measurement to evaluate the efficacy for pool boiling and flow boiling experiment. Pool boiling data was obtained while flow boiling is currently underway. The key findings of this study and future work are summarized below.

(1) MAND process can control the ZnO morphology by adjusting process parameters such as pH levels, reaction temperature, and residence time.

(2) Most of ZnO nanostructured surfaces in this study can significantly enhance the CHF as well as HTC in pool boiling performance.

(3) The unique nanostructured surface and the flower like surface showed the most enhanced heat transfer.

(4) ZSM-5 zeolite, which possesses very small pores, was not favorable for boiling performance due to pore property.

(5) Boiling phenomena were demonstrated in this pool boiling experiment, following conventional understanding.

(6) Two different ZnO morphologies, which were conducted in pool boiling experiment, were successfully synthesized in minichannel using the flow cell.

(7) Further investigations are needed to better understand the mechanism of ZnO nanoparticle deposition on plain substrates and minichannels.

(8) Experimental facility for convective flow boiling is required to evaluate the efficacy of the minichannels which are deposited with ZnO nanoparticles.

Reference

[1]. A Dewan1_, P Mahanta1, K Sumithra Raju1 and P Suresh Kumar, "*Review of passive heat transfer augmentation techniques*", Proc. Instn Mech. Engrs Vol. 218 Part A: J. Power and Energy pp.509.

[2]. Berenson P.J., "*Experiments on pool-boiling heat transfer*", Int. J. Heat Mass Transfer, Vol 5, pp. 985-999 (1962).

[3]. Gottzmann, C.F., Wulf, J.B., and O'Neill, P.S. "*Effect of surface characteristics on flow boiling heat transfer*", Proc. Conf. Natural Gas Research. Technology, Session V, paper 3, Chicago, IL (1971).

[4]. Kim, N.H. and Choi, K-K. " *Nucleate pool boiling on structured enhanced tubes having pores with connecting gaps*", Int. J. Heat Mass Transfer, Vol 44, pp. 17-28 (2001).

[5]. Lin, J.W., Lee, D.J., and Su, A., "*Metastable pin fin boiling*", Int. J. Heat Mass Transfer, Vol 44, pp. 241-246 (2001).

[6]. Bang, I.C., Chang, S.H., "*Boiling heat transfer performance and phenomena of Al2O3- water nano-fluids from a plain surface in a pool*", Int. J. Heat Mass Transfer, Vol 48, pp. 2407-2419 (2005).

[7]. Kim, H.D., Kim, J.B., and Kim, M.H., "*Experimental studies on CHF characteristics of nano-fluids at pool boiling*", Int.J. Multiphase Flow, Vol 33, pp.691-706 (2007).

[8]. Ujereh, S., Fisher T., and Mudaw, I., "*Effects of carbon nanotube arrays on nucleate pool boiling*", Int. J. Heat Mass Transfer, Vol 50, pp. 4023-4038 (2007).

[9]. Mudaw, I., "*Assessment of High-Heat-Flux Thermal Management Schemes*", IEEE Transaction on Components and Packaging Technologies, Vol 24 (2), pp. 122-410 (2001).

[10]. Qu, W. and Mudawar, I., "*Transport Phenomena in Two-Phase Micro-Channel Heat Sinks*", Proceedings of the ASME International Mechanical Engineering Congress & Exposition, paper #IMECE2002-33711, New Orleans, LA (2002).

[11]. Qu, W. and Mudawar, I., "*A methodology for Optimal Design of Two-Phase Micro-Channel Heat Sinks*", ASME, Vol 127, p.p 381(2005).

[12]. Qu, W. and Mudawar, I., "*Measurement and correlation of Critical Heat Flux in Two-Phase Micro-channel Heat Sinks*", International Journal of Heat and Mass Transfer, Vol 47, pp.2045 (2004).

[13]. Qu, W. and Mudawar, I., "*Measurement and Prediction of Pressure Drop in Two-Phase Micro-Channel Heat Sinks*", International Journal of Heat and Mass Transfer, Vol 46, pp. 2737 (2003).

[14]. Vikash, K., Mudawar, I., and Fisher, T., "*Flow Boiling in A Micro-Channel Coated with Carbon Nanotubes*", International Journal of Heat and Mass Transfer, Vol 52, pp. 3805 (2009).

[15]. Mitsutake, T. and Morooka, S., "*Boiling Heat Trasnfer Characteristics with Highly Wettable Heated Surface under Forced Convection Conditions*", JSME International Journal, Vol 47(2), pp. 168 (2004).

[16]. Nukiyama, S., J.japan Soc. Mech. Eng., Vol 37, pp. 367 (1934).

[17]. Forster. H.K., and Zuber, N., "*Dynamics of vapor bubbles and boiling heat transfer*", AIChE Journal, Vol 1, p.p 531 (1955).

[18]. Forster. H.K., and Greif, R., "*Heat transfer to a boiling liquid-mechanism and correlations*", ASME J.Heat Transfer, Vol 81, p.p 45 (1959).

[19]. Mikic,B.B., and Rohsenow, W.M., "*A new correlation of pool boiling data including the effect of heating surface characteristics*", ASME J.Heat Transfer, Vol 91, p.p 245 (1969).

[20]. Kutateladze, S.S., "*On the transition to film boiling under natural convection*", Kotloturbostroenie, Vol 3, p.p10 (1948).

[21]. Rohsenow, W.M., and Griffith, P., "*Correlation of maximum heat transfer data for boiling of saturated liquids*", Chem. Eng. Prog. Symp. Series, Vol 5, p.p 47 (1956).

[22]. Zuber, N., "*Hydrodynamic aspects of boiling heat transfer*", AEC Report AECU-4439, June, (1959).

[23]. Shulin JI and Changhui YE, "*Synthesis, Growth Mechanism, and Applications of Zinc Oxide Nanomaterials*", J. Mater. Sci. Technol., Vol 24(4), pp. 457 (2008).

[24]. Ahsanulhaq, Q. and Hahn, Y.B., "*Structural Properties and Growth Mechanism of Flower-like ZnO structure Obtained by Simple Solution Method"* , Material Research Bulletin, Vol 43, pp. 3483 (2008).

[25]. Ming Wang and Li-De Zhang, "*Synthesis of well-aligned ZnO nanorod arrays with high optical property via a low-temperature solution method*", Journal of Crystal Growth, Vol 291, pp. 334 (2006).

[26]. Changhui Ye and Dmitri Golberg, "*Thickness-Dependent Photocatalytic Performance of ZnO Nanoplatelets*", J. Phys. Chem. B, Vol 110, pp. 15146 (2006).

[27]. Vernardou, D. and Katsarakis, N., "*pH effect on the Morphology of ZnO nanostructures Grown with Aqueous Chemical Growth*", Thin Solid Films, Vol 515, pp. 8764 (2007).

[28]. Jung, J.Y., Ryu, S.O., and Chih-Hung Chang, "*The growth of the flower-like ZnO structure using a continuous flow microreactor*", Current Applied Physics, Vol 8(6), pp. 720 (2008).

[29]. Neelesh A. Patankar, "*Transition between superhydrophilic states on rough surface*", Langmuir, Vol 20, pp. 7097-7102 (2004).

[30]. Harvey, E.N., McElroy, W.D., and Whiteley, A.H., "*On cavity formation in water*, J.Appl.Phys, Vol 18, pp. 162 (1947).

[31]. Knapp, R.T., "*Cavitation and nuclei*", Trans.ASME, Vol 80, pp. 1315 (1958).

[32]. R.L. Webb, "*Nucleate boiling on porous coated surfaces*, Heat Transfer Eng., Vol 4, pp.71 (1983).

[33]. V. P. Carey, "*Liquid–Vapor Phase-Change Phenomena*": An Introduction to the Thermophysics of Vaporization and Condensation Processes in Heat Transfer Equipment, Taylor & Francis, London (1992).

[34]. L. S. Tong, Y. S. Tang, *Boiling Heat Transfer and Two Phase Flow*, Taylor & Francis, London (1997).

[35]. Renkun Chen, Ming-Chang Lu, and Arun Majumdar, "*Nanowires for enhanced boiling heat transfer*", Nano Letters, Vol 9, pp. 548 (2009).

[36]. Benjamin, J. and Garimella, S.,"*Infrared Micro-Particle Image Velocity Measurements and Predictions of Flow Distribution in a Microchannel Heat Sink*", International Journal of Heat and Mass Transfer, Vol 51, pp. 18 (2008).